

2D MULTI-ANGLE, MULTI-GROUP NEUTRINO RADIATION-HYDRODYNAMIC SIMULATIONS OF POSTBOUNCE SUPERNOVA CORES

CHRISTIAN D. OTT¹, ADAM BURROWS^{2,1}, LUC DESSART^{2,1}, AND ELI LIVNE³*Submitted to ApJ. March 31, 2008, accepted June 24, 2008.*

ABSTRACT

We perform axisymmetric (2D) multi-angle, multi-group neutrino radiation-hydrodynamic calculations of the postbounce phase of core-collapse supernovae using a genuinely 2D discrete-ordinate (S_n) method. We follow the long-term postbounce evolution of the cores of one nonrotating and one rapidly-rotating $20-M_\odot$ stellar model for ~ 400 milliseconds from 160 ms to ~ 550 ms after bounce. We present a multi-D analysis of the multi-angle neutrino radiation fields and compare in detail with counterpart simulations carried out in the 2D multi-group flux-limited diffusion (MGFLD) approximation to neutrino transport. We find that 2D multi-angle transport is superior in capturing the global and local radiation-field variations associated with rotation-induced and SASI-induced aspherical hydrodynamic configurations. In the rotating model, multi-angle transport predicts much larger asymptotic neutrino flux asymmetries with pole to equator ratios of up to ~ 2.5 , while MGFLD tends to sphericize the radiation fields already in the optically semi-transparent postshock regions. Along the poles, the multi-angle calculation predicts a dramatic enhancement of the neutrino heating by up to a factor of 3, which alters the postbounce evolution and results in greater polar shock radii and an earlier onset of the initially rotationally weakened SASI. In the nonrotating model, differences between multi-angle and MGFLD calculations remain small at early times when the postshock region does not depart significantly from spherical symmetry. At later times, however, the growing SASI leads to large-scale asymmetries and the multi-angle calculation predicts up to 30% higher average integral neutrino energy deposition rates than MGFLD.

Subject headings: Hydrodynamics, Neutrinos, Radiative Transfer, Stars: Evolution, Stars: Neutron, Stars: Supernovae: General

1. INTRODUCTION

Four decades after the first pioneering neutrino radiation-hydrodynamic calculations of stellar collapse (Colgate & White 1966; Arnett 1966; LeBlanc & Wilson 1970; Wilson 1971), the details of the core-collapse supernova explosion mechanism remain obscure. However, certain essentials are clear. The collapse of the evolved stellar core to a proton-neutron star (PNS) and its evolution to a compact cold neutron star provides a gigantic reservoir of gravitational energy, $\sim 3 \times 10^{53}$ erg, a mass-energy equivalent of $\sim 0.17 M_\odot$. Any core-collapse supernova mechanism must tap this energy and convert the fraction needed to match Type-II supernova observations ($\sim 10^{51}$ erg $\equiv 1$ Bethe [B]) into kinetic and internal energy of the exploding stellar envelope.

There is general agreement that the prompt hydrodynamic explosion mechanism does not work and that the bounce shock always stalls, falling short of blowing up the star (e.g., Bethe 1990; Janka et al. 2007), and must be re-energized to lead to a supernova. However, there is no agreement on the detailed mechanism that revives and endows the shock with sufficient energy to make a canonical ~ 1 -Bethe supernova.

For decades, the “neutrino-driven” mechanism, first proposed in its direct form by Colgate & White (1966), and in its delayed form by Wilson (1985) and Bethe & Wilson (1985), seemed compelling. It relies on a subtle imbalance of neutrino heating and cooling that leads to a net energy deposition behind the stalled shock, sufficient to revive it and drive the explosion on a timescale of hundreds of milliseconds. While appealing, it has been shown to fail for regular massive stars in spherical symmetry (1D) when the best neutrino physics and transport are used (Rampp & Janka 2000; Liebendörfer et al. 2001; Liebendörfer et al. 2005; Thompson et al. 2003). Yet, weak explosions may be obtained in 1D for the lowest mass progenitors, O-Ne-Mg cores (Kitaura et al. 2006; Burrows et al. 2007a).

It is now almost certain that the canonical explosion mechanism must be multi-dimensional (2D/3D) in nature. The multi-D dynamics associated with convective overturn in the postshock region (e.g., Herant et al. 1994; Burrows et al. 1995; Janka & Müller 1996; Buras et al. 2006a) and the recently identified standing accretion shock instability (SASI, e.g., Foglizzo & Tagger 2000; Foglizzo et al. 2007; Scheck et al. 2008; Blondin et al. 2003; Burrows et al. 2007c; Iwakami et al. 2008) lead to a dwell time of accreting outer core material in the postshock region that is larger on average than in the 1D case. This results in a greater neutrino energy deposition efficiency behind the shock and, thus, creates more favorable conditions for explosion (Burrows & Goshy 1993; Janka 2001; Thompson et al. 2005; Marek & Janka 2007).

¹ Department of Astronomy and Steward Observatory, The University of Arizona, 933 N. Cherry Ave., Tucson, AZ 85721; cott@as.arizona.edu, luc@as.arizona.edu

² Department of Astrophysical Sciences, Princeton University, Peyton Hall, Ivy Lane, Princeton, NJ 08544, burrows@astro.princeton.edu

³ Racah Institute of Physics, The Hebrew University, Jerusalem, Israel; eli@phys.huji.ac.il

The first generation of multi-dimensional supernova calculations, still employing gray flux-limited diffusion (or yet simpler schemes) for neutrino transport, indeed found that neutrino-driven convective overturn in the region between the stalled shock and the PNS sufficiently increased the neutrino energy deposition rate to lead to a delayed explosion (Herant et al. 1994; Burrows et al. 1995; Janka & Müller 1996; Fryer & Heger 2000; Fryer & Warren 2002, 2004). The more sophisticated studies that followed changed this picture. Recent long-term axisymmetric (2D) supernova calculations with multi-group, multi-species neutrino physics and transport find it difficult to explode garden-variety massive stars via the neutrino mechanism. Buras et al. (2006a) report explosion only for the low-mass ($11.2 M_{\odot}$) progenitor of Woosley et al. (2002), while Marek & Janka (2007) report the onset of explosion in a $15-M_{\odot}$ model of Woosley & Weaver (1995), given moderately fast rotation and the use of the Lattimer-Swesty equation of state (EOS; Lattimer & Swesty 1991) with a nuclear compressibility modulus K_0 of 180 MeV, which is significantly softer than the current best experimental values ($K_0 = 240 \pm 20$ MeV; Shlomo et al. 2006). On the other hand, Bruenn et al. (2006) obtain explosions for $11-M_{\odot}$ and $15-M_{\odot}$ progenitors from Woosley & Weaver (1995) only when they take silicon and oxygen burning into account and due to a synergy between nuclear burning, the SASI, and neutrino heating.

Burrows et al. (2006, 2007c) do not obtain neutrino-driven explosions (except in the case of O-Ne-Mg cores and accretion-induced collapse; Dessart et al. 2006b), but observe the excitation of PNS core g -modes. In their calculations, the PNS core oscillations reach non-linear amplitudes and damp via the emission of strong sound waves that propagate through the postshock region and efficiently deposit energy into the shock, eventually leading to late explosions at ~ 1 second after bounce. This *acoustic* mechanism appears to be robust enough to blow up even the most massive and extended progenitors (Burrows et al. 2007c; Ott et al. 2006a), but remains controversial and needs to be confirmed by other groups (see, e.g., Yoshida et al. 2007; Weinberg & Quataert 2008).

In the context of rapid progenitor rotation, Burrows et al. (2007b), Dessart et al. (2008), and Dessart et al. (2007) (the latter for the accretion-induced collapse scenario) have shown that energetic MHD-driven explosions may be obtained if field-amplification by the magneto-rotational instability (Balbus & Hawley 1991) is as efficient in the core-collapse context as suggested (Akiyama et al. 2003). Whether rotation alone and without strong magnetic fields favors or disfavors a neutrino-driven explosion remains to be seen (Walder et al. 2005; Dessart et al. 2006b; Ott et al. 2006b), but rapid rotation has been shown to damp convection (Fryer & Heger 2000) and weaken the SASI (Burrows et al. 2007b).

1.1. Core-Collapse Supernova Theory and Neutrino Radiation Transport

Neutrinos, their creation, propagation, and interactions with supernova matter, are of paramount importance to the core-collapse supernova problem. They carry away $\sim 99\%$ of the final neutron star's gravitational binding energy and $\sim 1\%$ of this energy would be sufficient to blow up the star. Depending on progenitor characteristics that set the postbounce rate of mass accretion onto the PNS, a successful supernova explosion should occur within ~ 1 – 1.5 s after bounce to match

observational and theoretical neutron star upper mass limits around ~ 2 – $2.5 M_{\odot}$ (Lattimer & Prakash 2007, and references therein). Consequently, the explosion mechanism must deliver canonical 1-B explosions on this timescale and, if the explosion is neutrino-driven, the neutrino heating efficiency⁴ must be on the order of 10% to yield an explosion that achieves an energy of 1 B within ~ 1 s.

The neutrinos travelling through the postshock region in a postbounce supernova core are not in thermal equilibrium with the baryonic matter. They should ideally be treated with full kinetic theory, describing the neutrino distributions and their temporal distribution with the Boltzmann equation (Mihalas & Mihalas 1984). Boltzmann transport is in its most general form a 7-dimensional problem. The 6D neutrino phase space (usually split up into 3D spatial coordinates, neutrino energy, and 2 angular degrees of freedom) and time. In addition, there are up to 6 neutrino types (3 particle species, and their anti-particles) to deal with. Spherically-symmetric Boltzmann transport schemes have been devised and implemented in the core-collapse context (Mezzacappa & Bruenn 1993a; Messer et al. 1998; Burrows et al. 2000; Yamada et al. 1999; Mezzacappa & Messer 1999; Rampp & Janka 2002; Liebendörfer et al. 2004; Hubeny & Burrows 2007), but general Boltzmann transport in multiple spatial dimensions is computationally challenging and will remain so in the intermediate term. Hence, approximations must be made in devising computationally tractable neutrino transport schemes for multi-D simulations.

A highly sophisticated approximation that arguably comes close to full Boltzmann transport in the case of quasi-spherical configurations in 2D is that presented in Buras et al. (2006b), and based on earlier work by Rampp & Janka (2002). These authors solve equations for the zeroth and first angular moments of spherically-symmetric radiation fields along multiple radial rays (ray-by-ray approach; Burrows et al. 1995) and perform a variable Eddington factor closure (Mihalas & Mihalas 1984) via a single spherically symmetric Boltzmann solution on an averaged 1D profile of the 2D hydrodynamics data. Neighboring rays are coupled to provide for limited treatment of latitudinal transport. Their multi-group (multi-energy and multi-neutrino species) scheme includes inelastic neutrino-electron scattering, aberration, gravitational redshift, and frame effects to $O(v/c)$.

Livne et al. (2004) implemented a genuinely 2D direct solution of a reduced Boltzmann equation via the method of discrete ordinates (S_n : see, e.g., Yueh & Buchler 1977; Mezzacappa & Bruenn 1993a; Adams & Larsen 2002; Castor 2004, and references therein) in the code VULCAN/2D, neglecting energy redistribution and fluid-velocity dependence.

A common, more approximate way to handle neutrino transport that has a long pedigree in 1D core-collapse studies is multi-group (energy/neutrino species) non-equilibrium flux-limited diffusion (MGFLD; Mihalas & Mihalas 1984, Arnett 1966, Bowers & Wilson 1982, Bruenn 1985, Myra et al. 1987; Myra & Burrows 1990; Baron et al. 1989; Cooperstein & Baron 1992). FLD schemes solve a diffusion equation for the mean radiation intensity, the zeroth angular moment of the specific radiation intensity. Hence,

⁴ We define the heating efficiency as the ratio of the energy deposition rate and the summed electron-neutrino and anti-electron neutrino luminosities. The μ and τ neutrinos and their anti-particles do not contribute much to the heating.

they drop all local angular dependence of the radiation field, while, in the MGFLD case, retaining the spectral neutrino distribution. MGFLD accurately describes the radiation field at high optical depth where the diffusion approximation is exact. In the free-streaming limit, the flux must be limited to maintain causality and an interpolation must be performed between diffusion and free-streaming regimes by an ad-hoc prescription (using a flux limiter).

2D FLD schemes were pioneered in the core-collapse context by LeBlanc & Wilson (1970) and modern MGFLD implementations can be found in Swesty & Myra (2006) and in Burrows et al. (2007c). It is not a priori clear whether MGFLD is an accurate enough prescription to yield post-bounce supernova dynamics in qualitative and quantitative agreement with a more accurate multi-angle treatment. Since net energy deposition by neutrinos is favored only in the semi-transparent gain layer, the quality of a MGFLD scheme may sensitively depend on the flux limiter chosen (Burrows et al. 2000). The fact that 2D gray FLD schemes have in the past led to neutrino-driven explosions (Herant et al. 1994; Burrows et al. 1995; Fryer & Heger 2000; Fryer & Warren 2002, 2004), while MGFLD schemes appear not to (Walder et al. 2005; Burrows et al. 2006, 2007c), emphasizes the importance of a spectral treatment of neutrino transport.

In 1D, MGFLD and Boltzmann neutrino transport were compared on static hydrodynamic postbounce backgrounds by Janka (1992), Yamada et al. (1999), Messer et al. (1998), and Burrows et al. (2000). Also in 1D, Mezzacappa & Bruenn (1993b) compared Boltzmann transport and MGFLD evolutions in the collapse phase, while Liebendörfer et al. (2004) performed the only comparison to date of 1D long-term Boltzmann and MGFLD supernova evolutions. The static studies all agree that Boltzmann transport yields larger instantaneous neutrino heating rates in the gain region, mostly because of a more slowly decreasing inverse flux factor (c over the ratio of flux to neutrino energy density), a quantity that can be related to the rate of energy absorption. On the other hand, Liebendörfer et al. (2004) find no significant dynamical differences between MGFLD and Boltzmann transport evolutions in their long-term comparison study with the 13- M_{\odot} progenitor model of Nomoto & Hashimoto (1988).

In this paper, we present 2D *multi-angle*, multi-group neutrino transport supernova calculations using the Newtonian axisymmetric VULCAN/2D code (Livne 1993; Livne et al. 2004; Burrows et al. 2007c). Comparing multi-D Boltzmann and MGFLD treatments, we perform postbounce simulations with VULCAN/2D and compare 2D steady-state snapshots, as well as fully-coupled dynamical 2D radiation-hydrodynamics evolutions, for non- and rapidly-rotating 20- M_{\odot} models whose precollapse profiles are taken from Woosley et al. (2002). We analyze our angle-dependent neutrino radiation fields and provide for the first time local 2D map projections of the specific intensity I_{ν} .

In §2, we describe our hydrodynamic and radiation-transport schemes and the microphysics that we use in this postbounce core-collapse supernova study. In §3, we introduce the presupernova models and the postbounce configurations, the setup, and the methodology of our Boltzmann-transport–MGFLD comparisons. In §4, we present results of snapshot Boltzmann transport calculations and compare them

with their MGFLD counterparts. In §5, we then discuss time-dependent calculations, the dynamical differences between Boltzmann transport and MGFLD runs, and the consequences for postbounce supernova model evolution. We wrap up in §6 with a summary and critical discussion of the work presented in this paper.

2. METHODS

2.1. Hydrodynamics

We employ the arbitrary Lagrangian-Eulerian (ALE, with second-order total-variation-diminishing [TVD] remap) radiation-hydrodynamics code VULCAN/2D. The hydrodynamics module was first described by Livne (1993)⁵. The 2D time-explicit hydrodynamics scheme is second-order accurate (in smooth parts of the flow), unsplit, and implements a finite-difference representation of the Newtonian Euler equations with artificial viscosity on arbitrarily structured grids and in cylindrical coordinates. The computational grid employed here is set up to resemble a spherical-polar grid at radii greater than 20 km and gradually transitions to a Cartesian structure at smaller radii (Ott et al. 2004). This (a) avoids hydrodynamic timestep restrictions due to focussing of angular grid lines and (b) liberates the PNS core, thus allowing mass motion along the axis of symmetry.

Self-gravity is implemented via direct grid-based solution of the Newtonian Poisson equation, as described in Burrows et al. (2007c), and we employ the finite-temperature nuclear equation of state of Shen et al. (1998a,b). The calculations are run with 230 logarithmically-spaced radial and 120 angular zones (including the inner, quasi-Cartesian region). The grid encompasses a radial extent of 4000 km and the full 180° of the axisymmetric domain.

2.2. Neutrino Transport and Microphysics

VULCAN/2D contains two multi-group, multi-species neutrino radiation-transport options. As we discuss below (§3), both modules are used in this study. The module implementing 2D transport in the MGFLD approximation, evolving the zeroth moment of the radiation field, is discussed in Burrows et al. (2007c). The angle-dependent transport module that evolves the specific neutrino radiation intensity, $I(\mathbf{r}, \Omega, \varepsilon_{\nu}, \text{species}, t)$, via the method of discrete ordinates (S_n), was first discussed by Livne et al. (2004) (see also Morel et al. 1996; Adams & Larsen 2002; Castor 2004).

For convenience and future reference, we define the zeroth, first, and second moments of the radiation field,

$$J_{\nu} \equiv \frac{1}{4\pi} \oint_{4\pi} d\Omega I_{\nu}, \quad (1)$$

$$\vec{H}_{\nu} \equiv \frac{1}{4\pi} \oint_{4\pi} d\Omega \vec{n} I_{\nu}, \quad (2)$$

$$\mathbf{K}_{\nu} \equiv \frac{1}{4\pi} \oint_{4\pi} d\Omega \vec{n} \vec{n} I_{\nu}. \quad (3)$$

Note the vector and tensor natures of \vec{H}_{ν} and \mathbf{K}_{ν} , respectively. \vec{n} is the radiation field unit vector whose coordinate-dependent

⁵ For details and an extension to magneto-hydrodynamics not employed here, see Livne et al. (2007).

components are given in Hubeny & Burrows (2007) for various common coordinate systems. Here we employ cylindrical coordinates (see Fig. 1). The radiation-pressure tensor K_ν obeys the trace condition $J_\nu = \text{Tr}[K_\nu]$ (Mihalas & Mihalas 1984). The spectral neutrino flux is defined as $\vec{F}_\nu = 4\pi\vec{H}_\nu$.

As explained in Livne et al. (2004), the time-implicit S_n solver in VULCAN/2D updates the specific intensity in the laboratory frame via the Boltzmann transport equation (Castor 1972) without fluid-velocity dependence,

$$\frac{1}{c} \frac{\partial I}{\partial t} + \vec{n} \cdot \vec{\nabla} I + \sigma I = S, \quad (4)$$

where we have dropped the neutrino group index ν . $\sigma = \sigma^a + \sigma^s$, where $\sigma^a(\mathbf{r}, \varepsilon_\nu, \text{species})$ is the inverse absorption mean-free path and $\sigma^s(\mathbf{r}, \varepsilon_\nu, \text{species})$ is the inverse scattering mean-free path (both equivalent to the corresponding cross section multiplied by the number density). We assume scattering to be isotropic and employ the transport cross section $\sigma^s = (1 - \langle \cos \vartheta \rangle) \sigma_T^s$ instead of the total scattering cross section σ_T^s . This approach has been shown to work well in spherically-symmetric core-collapse supernova calculations (Burrows et al. 2000; Thompson et al. 2003). The right-hand side source term S equals $S_{\text{em}}(\mathbf{r}, \varepsilon_\nu, \text{species}) + \sigma^s J$, where S_{em} is the emissivity. The transport grid is identical to the hydrodynamics grid. The specific intensity and its moments are defined at cell centers, facilitating spatially-consistent coupling with the scalar hydrodynamics variables, as discussed in Livne et al. (2004). Radiation stress at cell corners is computed via linear interpolation employing cell-centered values of the radiation flux.

As a consequence of the neglect of $O(v/c)$ terms in our transport formulation, neutrino advection, Doppler shifts and aberration effects are not considered. This greatly limits the computational complexity of the problem, but its impact on the transport solution depends on the particular choice of reference frame and was examined in Hubeny & Burrows (2007). It is clear that around core bounce and neutrino breakout, during the non-linear phase of the SASI hundreds of milliseconds after bounce, and in the case of rapid rotation, including $O(v/c)$ terms is advisable. We leave them out here in order to make long-term multi-angle radiation-hydrodynamics simulations feasible and allow direct comparison with the MGFLD variant of VULCAN/2D. Full $O(v/c)$ Boltzmann transport with energy redistribution will be addressed using the code BETHE currently under development by a subset of our group (Hubeny & Burrows 2007; Murphy & Burrows 2008).

We discretize the angular radiation distribution evenly in $\cos \vartheta$ from -1 to 1 and in φ evenly from 0 to π (treating only one hemisphere because of axial symmetry). We make the number of φ -bins a function of $\cos \vartheta$ to tile the hemisphere more or less uniformly in solid angle. In our time-dependent runs we employ 8 $\cos \vartheta$ bins, resulting in a total of 40 angular zones. Steady-state radiation fields are computed with 8 $\cos \vartheta$ bins, 12 $\cos \vartheta$ bins (92 total angular zones) and 16 $\cos \vartheta$ bins (162 total angular zones) at each spatial grid point.

The standard set of neutrino-matter interactions listed in Thompson et al. (2003) is included and all computations are performed with 16 discrete neutrino energy bins, approximately logarithmically spaced from 2.5 MeV to 220 MeV. Electron neutrinos (ν_e) and electron-antineutrinos ($\bar{\nu}_e$) are

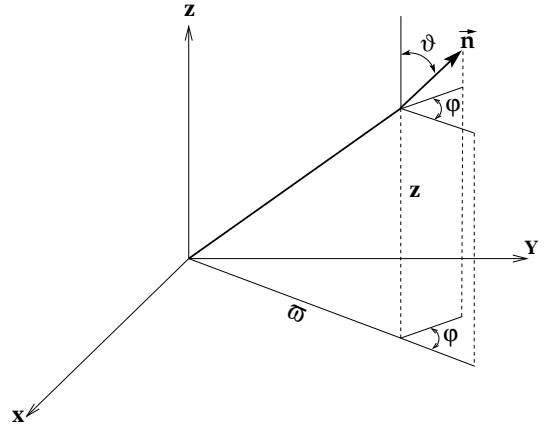


FIG. 1.— Coordinates used in the axisymmetric S_n transport scheme implemented in VULCAN/2D. The radiation direction vector \vec{n} is defined in terms of ϑ and φ . ϑ is the angle with respect to the coordinate-grid z -axis at all spatial positions (z, ϖ) . At each (z, ϖ) , the local momentum-space unit sphere is covered by n zones in ϑ and at each ϑ location by a number $m(\vartheta)$ of φ -zones, so that each zone in (ϑ, φ) covers roughly the same solid angle.

treated independently while we lump together the heavy-lepton μ , $\bar{\mu}$, τ , and $\bar{\tau}$ neutrinos into one group (“ ν_μ ”). The code is very efficiently parallelized via MPI in energy groups and species. As an additional simplification, we do not include energy redistribution by inelastic neutrino-electron scattering. Such energy redistribution and scattering are of modest ($\sim 10\%$) relevance for the trapped electron fraction (Y_e) and entropy of the inner core at core bounce, but otherwise arguably quite subdominant (Thompson et al. 2003).

2.3. A Hybrid Approach – Combining S_n and MGFLD Neutrino Transport

The time-implicit S_n scheme in VULCAN/2D is iterative and suffers convergence problems in regions where the transport problem is scattering-dominated and the optical depth is high ($\tau \gtrsim 5$). As a consequence, Livne et al. (2004) limited the timestep at postbounce times to ~ 0.1 – $0.3 \mu\text{s}$ to ensure accuracy and stability. In the present study, we take a different approach and introduce a hybrid S_n –MGFLD transport scheme that treats the quasi-isotropic transport problem in the optically-thick PNS interior in the diffusion approximation and transitions to full multi-angle S_n transport in a region of moderate optical depth ($\tau \gtrsim 2$), but that is still significantly interior to the neutrinospheres ($\tau \sim 2/3$) where the neutrinos decouple from matter and begin to stream.

We chose a radius of 20 km in our calculations for the transition from MGFLD to S_n . This is a sensible choice, (1) because the neutrinosphere radii of all groups (energies/species) remain larger than 20 km throughout the postbounce period our simulations cover and, (2) because 20 km also marks the radius at which the transition from the inner irregular quasi-Cartesian grid to the outer regular grid is complete. This boundary is smooth and the S_n –MGFLD transition does not suffer from Cartesian cornerstone effects.

The transition is implemented by setting up for each energy group and species an approximate specific intensity I_ν at the centers of the zones below the S_n –MGFLD interface using the information available from MGFLD. This approximate I_ν is obtained via its angular expansion to first order in \vec{n} (the Eddington approximation):

$$I_\nu = I_0 + 3(\vec{n} \cdot \vec{H}). \quad (5)$$

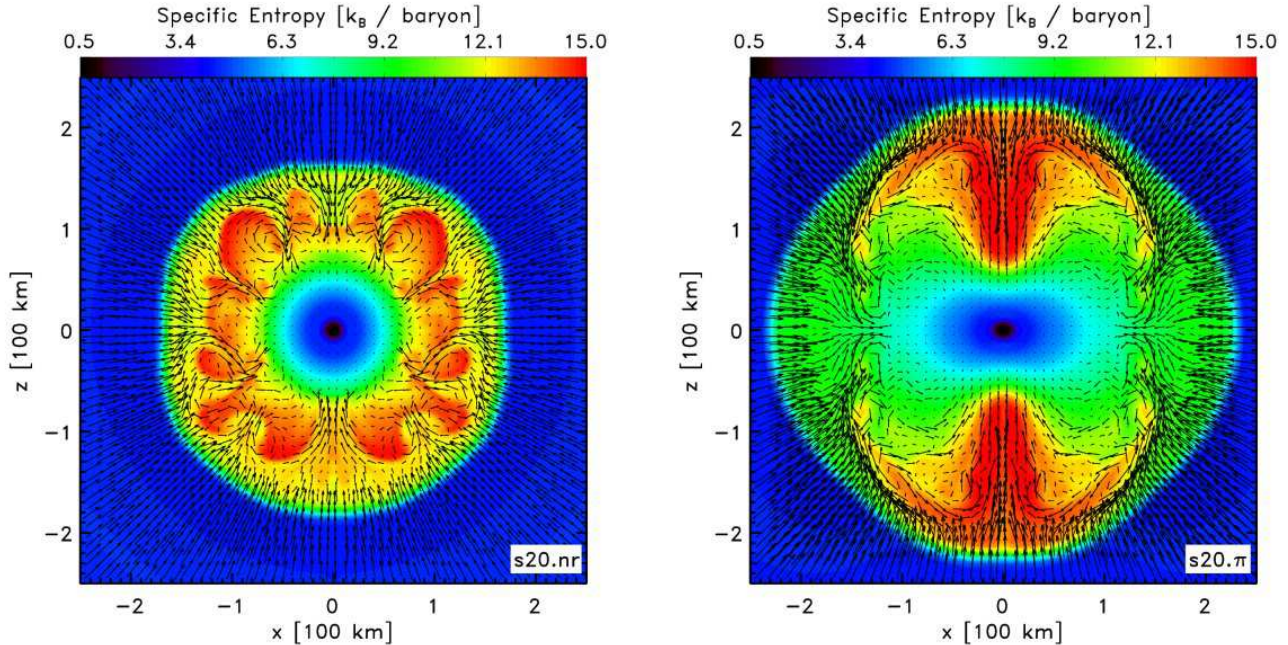


FIG. 2.— Entropy colormaps of the nonrotating model s20.nr (left) and the rotating model s20.π (right) at 160 ms into their postbounce evolution computed with MGFLD. Velocity vectors are superposed with vector lengths saturated at $1.0 \times 10^9 \text{ cm s}^{-1}$. Model s20.nr has a practically spherical PNS and shows features of violent overturn in the convectively unstable postshock region. The shock radius in this model is $\sim 175 \text{ km}$ at this point and the onset of the SASI is apparent from the slightly deformed shock. Model s20.π, on the other hand, has a strongly rotationally-flattened PNS and convective overturn is confined to polar regions. These regions exhibit the globally highest entropies and greatest entropy gradients, since the polar velocity divergence at the shock is the highest. The shock radius at this time in model s20.π is $\sim 230 \text{ km}$ and no SASI features are visible.

Here, $I_0 = J_{\text{MGFLD}}$ and $\vec{H} = \vec{F}_{\text{MGFLD}}/4\pi$, where \vec{F}_{MGFLD} is the flux, and \vec{H} is the first moment of I_ν . In MGFLD, \vec{F}_{MGFLD} is computed via

$$\vec{F}_{\text{MGFLD}} = -\text{FL}[D]\vec{\nabla}J, \quad (6)$$

where

$$D = \frac{1}{3\sigma}, \quad (7)$$

with Bruenn's flux limiter⁶ (Bruenn 1985),

$$\text{FL}[D] = \frac{D}{1 + D|\vec{\nabla}J|/J}. \quad (8)$$

The first angular moment of eq. (5), $\vec{F}_{S_n} = \int \vec{n} I d\Omega$, is then equal⁷ to \vec{F}_{MGFLD} and the S_n -MGFLD matching is consistent and provides a representation of the specific intensity I that is accurate to first order in \vec{n} . Given the essentially isotropic neutrino radiation field deep inside the PNS, this approximation yields excellent results. We note that the scheme makes the implicit assumption that the radial gradient of the mean intensity at the transition radius is always negative or zero. This condition is generally fulfilled in PNSs.

3. INITIAL MODELS AND SETUP

⁶ We use Bruenn's flux limiter in VULCAN/2D, because Burrows et al. (2000) found it to perform best in their comparison of flux limiters with angle-dependent transport.

⁷ Given the limited number of angular zones of I and the fact that we are not using Gaussian-quadrature-type angular zoning, the integrals of I are only accurate to $\sim 5\%$ when 8 ϑ -zones are used and accurate to $\sim 1\%$ when 12 and more ϑ -zones are employed. To ensure conservation of energy in the S_n -MGFLD matching, we employ purely geometrical and temporally constant correction factors to enforce $\vec{F}_{S_n} = \vec{F}_{\text{MGFLD}}$ at the interface.

We employ the spherically-symmetric solar-metallicity $20\text{-}M_\odot$ (at ZAMS) model s20.0 from the stellar evolutionary study of Woosley et al. (2002), who evolved it to the onset of core collapse. At that moment, its iron core mass⁸ is $\sim 1.46 M_\odot$ and its central density has reached $\sim 8.4 \times 10^9 \text{ g cm}^{-3}$. A graph of the progenitor's precollapse density stratification as a function of enclosed mass can be found in Fig. 1 of Burrows et al. (2007c). Note that in the study of Woosley et al. (2002), iron core mass and extent vary non-monotonically in the $10\text{-}20 M_\odot$ ZAMS mass range and that their solar-metallicity $20\text{-}M_\odot$ model has, in fact, a more compact central configuration than the corresponding $15\text{-}M_\odot$ model. Stellar evolution theory of massive stars has yet to converge and studies by different groups do not presently yield the same presupernova structures.

We set up two initial models in VULCAN/2D: s20.nr and s20.π. Both models are mapped from 1D onto our 2D hydrodynamic grid under the assumption of spherical symmetry. Model s20.nr is kept nonrotating, while we impose an initial angular velocity profile in model s20.π according to the rotation law,

$$\Omega(\varpi) = \Omega_0 \frac{1}{1 + (\varpi/A)^2}, \quad (9)$$

where ϖ is the distance from the rotation axis and A is a parameter governing precollapse differential rotation. This rotation law enforces constant angular velocity on cylindrical shells and, for sensible choices of A , reproduces qualitatively (Ott et al. 2006b) predictions from presupernova models that include rotation in a 1D fashion (Heger et al. 2000, 2005). Since the computational complexity of this study inhibits us

⁸ Determined by the discontinuity in the electron fraction, Y_e , at the outer edge of the iron core where $Y_e \sim 0.5$.

from performing a sweep of the Ω_0 - A parameter space, we chose $A = 1000$ km and $\Omega_0 = \pi$ rad s $^{-1}$. Hence, the initial central period is 2 s – this is an identical rotational setup to the fiducial model in Burrows et al. (2007b). As discussed in Ott et al. (2006b), 2 s is rather short, leads to a rapidly rotating postbounce configuration with a millisecond-period PNS, and, unless significant postbounce spin-down (e.g. via MHD torques) occurs, is inconsistent with average pulsar birth spin estimates. We chose such rapid rotation simply because we wish to study a postbounce supernova core with significant rotationally-induced asymmetry. Key model parameters and characteristics are summarized in Table 1.

We collapse both models with the MGFLD variant of VULCAN/2D and evolve them to ~ 160 ms after core bounce. Then, we transition to S_n Boltzmann transport and solve for the stationary neutrino radiation field based on the artificially frozen hydrodynamics data at this postbounce time. Once we have obtained a converged angle-dependent radiation field, we activate neutrino-matter coupling and hydrodynamics and evolve in time the coupled radiation-hydrodynamics equations. For direct comparison, we also continue the MGFLD simulations to later times. All steady-state snapshots are computed in three momentum-space angular resolutions, S_{16} , S_{12} , and S_8 , while the long-term evolution calculations could only be performed with S_8 , due to computational constraints.

In Fig. 2, we show entropy colormaps of both models at 160 ms after bounce. Fluid velocity vectors are superposed, providing a snapshot of the flow. By 160 ms after bounce, in the nonrotating model s20.nr convection in the high-entropy ($O(10)$ k $_B$ /baryon) gain layer has developed fully. The shock sits at ~ 175 km and is slightly deformed by the onset of the SASI. Not visible on the scale of this figure is the lepton-gradient-driven convective region deep inside the PNS, which was extensively discussed in Dessart et al. (2006a).

The PNS in the rapidly rotating model s20. π is rotationally flattened, with unshocked low-entropy inner-core pole/equator asymmetry ratios below ~ 0.5 . The shock is slightly prolate and has attained an average radius of ~ 230 km. The moment-of-inertia-weighted mean period of the unshocked (specific entropy $s \leq 3$ k $_B$) inner core is ~ 2.0 ms. Differential rotation between ~ 20 and 200 km is very large, with the angular velocity Ω dropping from ~ 1600 rad s $^{-1}$ to a mere ~ 15 rad s $^{-1}$ over this radial equatorial interval. Yet, the specific angular momentum j is still monotonically and rapidly increasing. It flattens, but does not decrease, only at radii greater than ~ 100 km. This positive gradient in j stabilizes the postbounce core against convective instability at low latitudes (Fryer & Heger 2000), confining overturn to the polar regions and large equatorial radii where the j gradient is less steep.

4. RESULTS: SNAPSHOTS

In this section, we present our S_n multi-angle transport results for steady-state model snapshots at 160 ms after core bounce. We diagnose the angle-dependent neutrino radiation fields and carry out a comparison between multi-angle and MGFLD transport results based on local and global radiation-field variables.

TABLE 1
MODEL SUMMARY

Model Name	Progenitor	Ω_0 (rad s $^{-1}$)	A (km)	t_b (ms)	t_{snap} (ms)	$t_f - t_b$ (ms)
s20.nr	s20.0	0.0	—	179.2	160.0	500.0
s20. π	s20.0	π	1000	193.7	160.0	550.0

NOTE. — Summary of model parameters. The progenitors are taken from Woosley et al. (2002). Ω_0 is the initial central angular velocity, A is the differential rotation parameter of the rotation law (eq. 9). t_b is the time of core bounce, t_{snap} is the time after t_b at which the postbounce snapshots are taken, and $t_f - t_b$ is the point at which we stop our simulations.

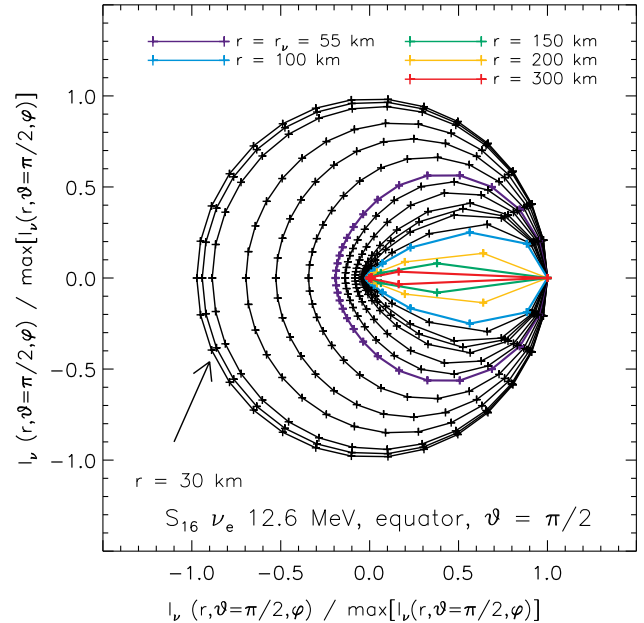


FIG. 3.— Polar plot of the normalized specific intensity $I_\nu(r, \vartheta, \varphi) / \max[I_\nu(r, \vartheta, \varphi)]$ in model s20.nr at 160 ms after core bounce, at selected equatorial radii, and for ν_e neutrinos at $\varepsilon_\nu = 12.6$ MeV. At each radius, we normalize the specific intensity by its local maximum. Shown is the variation with φ at fixed $\vartheta = \pi/2$. The graphs are based on a S_{16} calculation. At $r = 30$ km, the radiation field is practically isotropic, but is already appreciably forward-peaked at the neutrinosphere ($r_\nu = 55$ km; optical depth $\tau = 2/3$) and thereafter smoothly transitions over ~ 200 – 300 km to the free-streaming limit.

4.1. Angular Distributions

The quintessential problem in treating neutrino radiation transport in core-collapse supernova cores is the fact that the neutrino transport mean-free path, the average distance a neutrino can travel without experiencing scattering or absorption, changes by orders of magnitude from inside to outside. Moreover, the neutrino transport mean-free-path λ_ν varies locally strongly with neutrino energy ($\propto \varepsilon_\nu^2$) and matter density. As a consequence, gray transport schemes are problematic, since neutrino-energy averages can be defined only locally and the mean neutrino energy varies significantly throughout the supernova core.

From a more geometric point of view, the radiation field in momentum space goes from being completely isotropic (net flux \sim zero) to being focussed into the radial direction (“forward-peaked”) in the free-streaming regime. In the MGFLD approximation, the mean intensity J_ν is evolved in time and the angular information, in particular the informa-

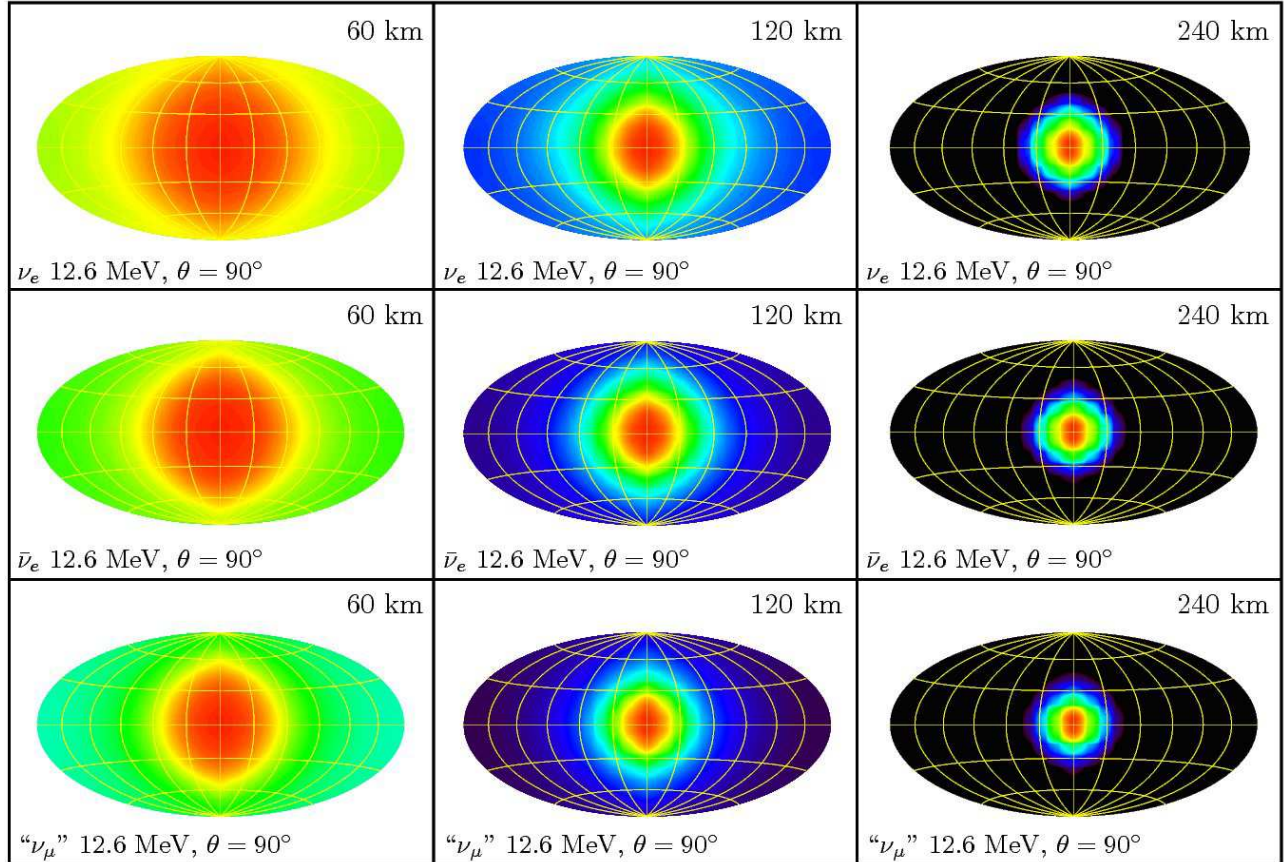


FIG. 4.— Hammer-type interpolated (smoothed) map projections of the normalized specific intensity $I_\nu(\vartheta, \varphi)/J_\nu$ in model s20.nr at 160 ms after bounce. The colormap is logarithmic and in each individual projection is setup to range from $\max(I_\nu(\vartheta, \varphi)/J_\nu)$ (red) to $10^{-4}\max(I_\nu(\vartheta, \varphi)/J_\nu)$ (black). Shown is the specific intensity of ν_e , $\bar{\nu}_e$, and “ ν_μ ” neutrinos at $\varepsilon_\nu = 12.6$ MeV (rows) on the equator ($\theta=90^\circ$, measured from the pole) and at radii of 60, 120, and 240 km (columns). The Hammer projection is set up in such a way that ϑ varies in the vertical from 0° (top) to 180° (bottom) and φ varies horizontally from -180° (left) to $+180^\circ$ (right). Grid lines are drawn in ϑ - and φ -intervals of 30° . Note (a) the increasing forward-peaking of I_ν with increasing radius (and decreasing optical depth) and (b) that at any given radius I_ν of “ ν_μ ” is more forward-peaked than that of the $\bar{\nu}_e$ component, which, in turn, is always more forward-peaked than the ν_e component. This fact is a consequence of a transport mean-free path that varies with species (and energy; not shown here) and is smallest for the electron neutrinos.

tion on the degree of forward-peaking, is captured only by computing spatial gradients in J_ν and employing a flux limiter to interpolate between diffusion and free streaming.

The S_n Boltzmann solver in VULCAN/2D is able to self-consistently handle the transition from isotropic to forward-peaked radiation. Figure 3 depicts the angular distribution in the azimuthal angle φ (see Fig. 1) of the normalized specific spectral neutrino intensity I_ν for electron neutrinos at 12.6 MeV. In Fig. 3, the polar angle ϑ is set equal to $\pi/2$ and the φ -distribution is given at various radii in the equatorial plane of model s20.nr. At 30 km from the center, the radiation field of ν_e 's at $\varepsilon_\nu = 12.6$ MeV is nearly isotropic, which corresponds to a circle in Fig. 3. With increasing radius (and, of course, decreasing matter density) the transport mean-free path at fixed ε_ν increases and the radiation field gradually departs from isotropy and becomes more and more forward-peaked. We define the neutrinosphere as the surface at which the optical depth τ_ν , given by

$$\tau_\nu = \int_\infty^R \frac{dr}{\lambda_\nu}, \quad (10)$$

is equal to $2/3$. At around this τ_ν , the neutrinos decouple from matter and begin to stream freely. At 160 ms after bounce in model s20.nr, the 12.6 MeV ν_e neutrinosphere is located

at $r \sim 55$ km. As is obvious from Fig. 3, the radiation field at the neutrinosphere is not yet dramatically forward-peaked, but becomes so with increasing radius. However, complete forward-peaking only obtains at radii $\gtrsim 250$ – 300 km, beyond which the angular resolution of our S_n scheme becomes sub-optimal, even with $n = 16$. However, calculations with varying number of ϑ (and, hence, φ) angles reveal that the transition from isotropy to moderate and large anisotropy is adequately reproduced at small and intermediate radii (out to ~ 200 km) even in the case of S_8 .

For the purpose of displaying and studying the local neutrino radiation field, we provide equal-area Hammer-type map projections (Hammer 1892). Such map projections are new to the field of neutrino radiation transport and beautifully reveal the multi-D angular-dependence of the radiation field. In Fig. 4, we present such Hammer projections on the equator (spatial $\theta = 90^\circ$) of model s20.nr at radii of 60, 120, and 240 km for the three neutrino species included in our simulations at $\varepsilon_\nu = 12.6$ MeV. In each plot, we normalize the specific intensity to the mean intensity to set a common scale. The colormap is logarithmic and chosen to have regions on the sphere with high intensity appear red and regions of low intensity appear black.

For neutrinos on the equator, the momentum-space forward

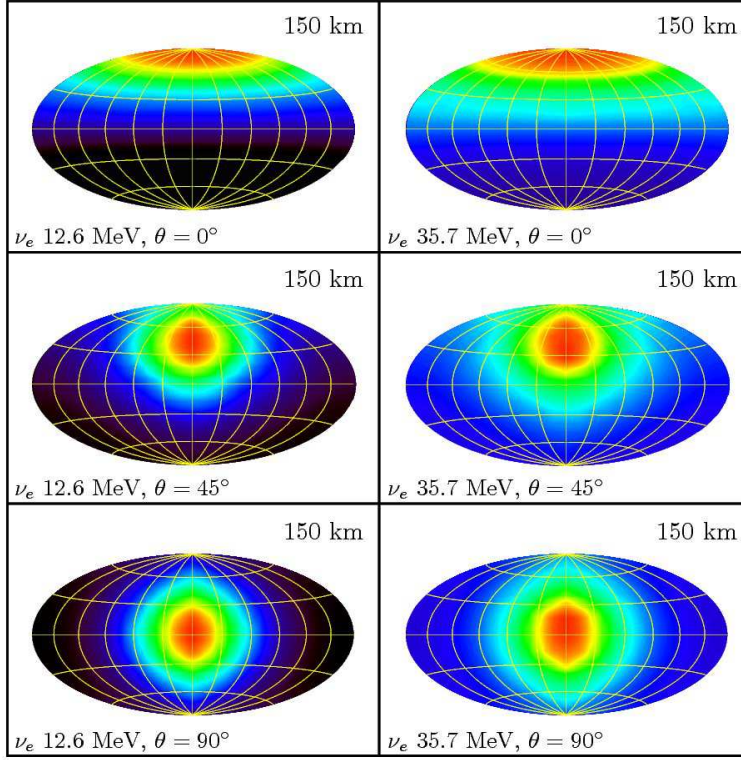


FIG. 5.— Hammer map projections of the interpolated (smoothed) normalized specific intensity $I_\nu(\vartheta, \varphi)/J_\nu$ at 160 ms postbounce in model s20.nr. The projections are set up in identical fashion to Fig. 4. Shown here is the variation of the angular distribution with energy group (columns) and angular position (rows) for electron neutrinos. The radius is fixed to 150 km. As expected in the coordinates used for the S_n transport in VULCAN/2D (see Fig. 1), I_ν becomes forward-peaked into $\vartheta = 0^\circ$ and degenerate in φ along the pole ($\theta = 0^\circ$), forward-peaked into $\vartheta = 45^\circ, \varphi = 0^\circ$ on the diagonal ($\theta = 45^\circ$), and forward-peaked $\vartheta = 90^\circ, \varphi = 0^\circ$ on the equator ($\theta = 90^\circ$). The degree of the radiation anisotropy and its variation from forward-peaked at $\varepsilon_\nu = 12.6$ MeV to less forward-peaked at $\varepsilon_\nu = 37.5$ MeV is apparent.

direction is ($\vartheta = 90^\circ, \varphi = 0$). Electron neutrinos generally have the shortest transport mean-free path of all species in the core-collapse context and decouple from matter at the lowest densities. The Hammer projection in the top-left corner of Fig. 4 of the $\varepsilon_\nu = 12.6$ MeV equatorial radiation field at 60 km corresponds roughly to the blue line graph in Fig. 3, which portrays only its variation with φ . At fixed neutrino energy group ε_ν , electron anti-neutrinos and “ ν_μ ” neutrinos decouple at smaller radii. Hence, as Fig. 4 shows, at 60 km, they already manifest greater local anisotropy than the ν_e s. This trend continues at all considered radii in Fig. 4.

In Fig. 5, we again present Hammer projections of the normalized specific intensity, but this time consider only ν_e s, keep the radius fixed at 150 km, and vary the neutrino energy and the angular position on the grid. The bottom row of Fig. 5 shows the normalized I_ν at the equator ($\theta = 90^\circ$) and for the 12.6-MeV and 35.7-MeV ν_e energy groups. The center and top rows show the same groups at $\theta = 45^\circ$ and at $\theta = 0^\circ$, respectively. From the discussion of Fig. 4, we are already familiar with the overall radiation field geometry. The transport mean-free path scales roughly inversely with ε_ν^2 . Hence, at any given position in the postbounce supernova core, more energetic neutrinos should be locally more isotropically distributed in momentum space than less energetic ones. The less forward-peaked angular I_ν distribution of the higher-energy neutrinos reflects this.

The degree of forward-peaking in ϑ and φ of the radiation field in the quasi-spherically symmetric nonrotating model s20.nr is essentially independent of the angular position on the grid and the radiation fields at any given radius can be

transformed into one another by simple rotation. Because of the aspherical and oblate distribution of matter in the rotating model s20. π , the forward-peaking is also a function of polar angle. Due to its PNS’s oblateness (see Fig. 2), the neutrinos generally decouple at significantly smaller radii near the pole than near the equator, in turn leading to more strongly forward-peaked radiation fields in the polar than in the equatorial regions (Janka & Muenchmeyer 1989a,b; Walder et al. 2005; Dessart et al. 2006b, 2007).

4.2. Eddington Factors

The radiation-pressure tensor K_ν , also known as the Eddington tensor, represents the second angular moment of the specific intensity and is defined by eq. (3). In the following, we use its normalized variant $k_\nu = K_\nu/J_\nu$.

In spherical symmetry, k_ν is diagonal and has a single independent component, the Eddington factor k_ν . For isotropic radiation, $k_\nu = 1/3$ and $K_\nu = \text{diag}(1/3, 1/3, 1/3)$, while in the streaming regime, $k_\nu = 1$ and $K_\nu = \text{diag}(1, 0, 0)$. In the transition from isotropy to free streaming, k_ν generally varies from $1/3$ to 1 , but in special cases, e.g., enhanced radiation perpendicular to the radial direction, may assume values below $1/3$. Note that one of the common assumptions of MGFLD is the Eddington closure, setting $k_\nu = \frac{1}{3}$ everywhere.

In axisymmetry and ignoring velocity-dependent terms, the Eddington tensor has four independent components whose individual meaning depends on the coordinates chosen⁹. We

⁹ Off-diagonal components of the Eddington tensor can be related to ra-

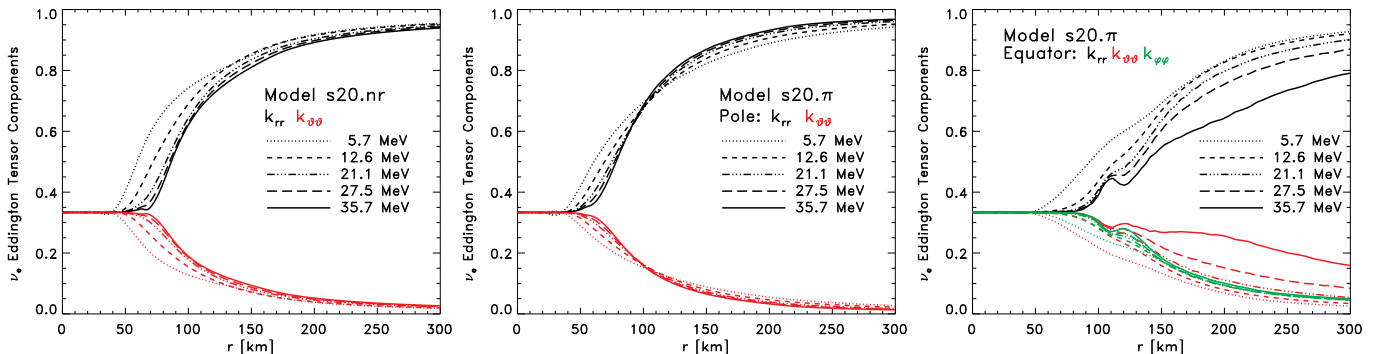


FIG. 6.— Normalized Eddington tensor k components in spherical coordinates as a function of neutrino energy ε_ν and spherical radius r . **Left:** Angular-averaged k_{rr} and $k_{\vartheta\vartheta}$ for electron neutrinos in model s20.nr. $k_{\varphi\varphi}$ is not shown, but has essentially identical behavior to $k_{\vartheta\vartheta}$. The diagonal components start out with $1/3$ at small radii, as expected for the prevailing isotropic radiation fields. With increasing radius (and decreasing density), the local radiation field becomes more anisotropic and forward-peaked. This occurs at progressively larger radii with increasing ε_ν and is reflected by the increasing k_{rr} and the decreasing $k_{\vartheta\vartheta}$ in the plot. The off-diagonal component $k_{r\vartheta}$ is not shown, does not exhibit clear systematics, and is generally a factor of 10–100 smaller than the diagonal components. **Center:** Same as left, but showing profiles extracted from regions near the pole in the rapidly-rotating model s20. π . Interior to ~ 100 km, k_{rr} , and $k_{\vartheta\vartheta}$ show the same systematics with ε_ν as in the nonrotating model. However, at larger radii they are reversed, k_{rr} and $k_{\vartheta\vartheta}$ exhibiting greater isotropy for lower ε_ν . See text for discussion. **Right:** Equatorial profiles of k_{rr} , $k_{\vartheta\vartheta}$ and $k_{\varphi\varphi}$ for electron neutrinos in model s20.nr. Due to rotational flattening of the PNS, the transition to free streaming occurs over a much larger range of radii near the equator. $k_{\vartheta\vartheta}$ shows a significantly larger variation as a function of energy than $k_{\varphi\varphi}$.

assume and transform to spherical coordinates for our discussion, since they make the interpretation of the components most straightforward.

In Fig. 6, we present radial profiles of normalized Eddington tensor components at selected electron-neutrino energies ε_ν in models s20.nr and s20. π . The nonrotating model can be considered nearly spherically symmetric, and, hence, should and does exhibit the expected Eddington-factor systematics. At small radii and high densities, where neutrinos and matter are in equilibrium, $k_{rr} = k_{\vartheta\vartheta} = k_{\varphi\varphi} = \frac{1}{3}$ and with increasing radius, $k_{rr} \rightarrow 1$ and $\{k_{\vartheta\vartheta}, k_{\varphi\varphi}\} \rightarrow 0$. As expected from the basic decoupling hierarchy, the value of the Eddington tensor components is a strong function of ε_ν . Lower- ε_ν neutrinos decouple at higher densities, and, hence, have Eddington tensor components which depart from $\frac{1}{3}$ at smaller radii than ν_e s and “ ν_μ ”s as well. The off-diagonal component $k_{r\vartheta}$ is zero in the isotropic region, does not exhibit clear systematics, and stays an order-of-magnitude smaller than the diagonal components for all ε_ν and species.

The rotating model s20. π has a postshock configuration that is far from spherically symmetric (Fig. 2). We present in Fig. 6 separate plots for its Eddington tensor components in regions near the pole and near the equator. In the polar regions and at small radii ($r \lesssim 100$ km), the Eddington tensor components show the same qualitative behavior as in model s20.nr. At larger radii, however, the systematics are reversed and lower- ε_ν electron neutrinos have more isotropic radiation fields (smaller k_{rr}) than their higher- ε_ν counterparts. Analyzing their radiation fields and matter coupling in detail, we find that this surprising feature is a consequence of electron capture and the polar compactness (large density gradient due to rotation) of the supernova core. Electron capture near the shock leads to isotropic neutrino emission that can locally isotropize the radiation field in semi-transparent regions. With decreasing density and temperature, the mean energy of neutrinos emitted by capture processes shifts to lower ε_ν . This leads to greater local isotropization of lower- ε_ν neutrinos, which in turn is reflected in the more slowly increas-

ing radiation shear viscosity (Mihalas & Mihalas 1984), which we do not consider here.

ing k_{rr} of these neutrinos. This interpretation is confirmed by the fact that we do not find any such feature in the Eddington tensor components of the “ ν_μ ” neutrinos that are not produced in capture processes. We also do not observe significant isotropization in the $\bar{\nu}_e$ radiation fields, since the emission of $\bar{\nu}_e$ s by positron capture on neutrons is weaker due to the lower positron abundance.

In regions of model s20. π near the equator where the PNS is most extended, the neutrino radiation fields stay isotropic to large radii and decouple from matter only slowly with radius. Since the matter densities in the equatorial plane stay roughly a factor of four larger than in the polar regions, the cross-over feature in $\{k_{rr}, k_{\vartheta\vartheta}, k_{\varphi\varphi}\}$ does not appear and these components follow the standard decoupling hierarchy. Interestingly, and different from in the nonrotating model, $k_{\vartheta\vartheta}$ and $k_{\varphi\varphi}$ show quantitatively distinct variation with ε_ν , the latter exhibiting significantly less variation with ε_ν at any given radius. The interpretation of this observation is not straightforward, but we suggest that it can be attributed to the fact that in model s20. π the radiation field at any given point on the equator of the rotationally-flattened core and for any ε_ν and neutrino species varies locally less in the ϑ direction than in the φ direction. This, in combination with the fact that on the equator the radiation field asymptotically peaks into the ($\vartheta = 0, \varphi = 0$) direction, results on average in smaller $k_{\varphi\varphi}$ with less spread in energy than exhibited by $k_{\vartheta\vartheta}$. The off-diagonal component $k_{r\vartheta}$ (not shown in Fig. 6) vanishes in $k_{rr} = k_{\vartheta\vartheta} = k_{\varphi\varphi} = \frac{1}{3}$ regions, but can become relatively large at greater radii (up to ~ 0.2 in magnitude; increasing with ε_ν and radius) and flips sign at the equator. The interpretation of $k_{r\vartheta}$ is not straightforward, since its magnitude depends on the choice of coordinates. We do not attempt to study it, nor its implications for neutrino shear viscosity, in any detail.

4.3. Global Radiation Field Diagnostics: Luminosities, Spectra, Flux Factors, and Neutrino Energy Deposition

So far we have studied aspects of neutrino transport inaccessible to MGFLD. We now go on to discuss radiation field diagnostics that facilitate a S_n –MGFLD comparison. For further reference and comparison with previous studies (Janka 1992; Messer et al. 1998; Burrows et al. 2000), we define the

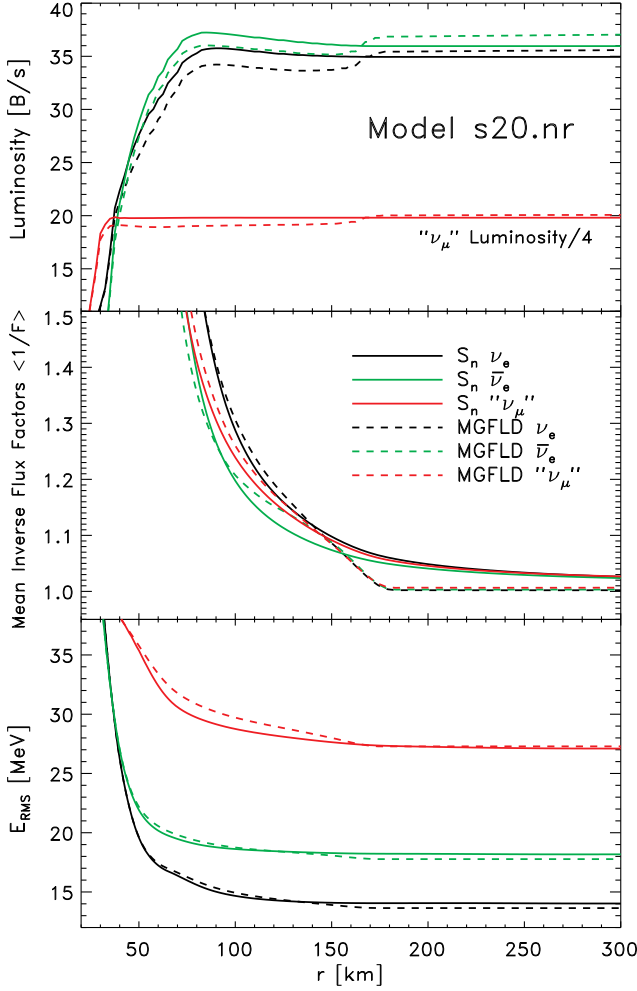


FIG. 7.— S_n –MGFLD comparison for the nonrotating model s20.nr at 160 ms after bounce. All S_n results were obtained with a 16 ϑ -angle calculation. See text for details and discussion. Top panel: Neutrino luminosity as a function of radius and broken down into the three neutrino species considered. The “ ν_μ ” neutrinos dominate in luminosity and their luminosity profiles are scaled by a factor of 1/4 to preserve the overall scale of the plot. Center panel: Angle-averaged energy-mean inverse neutrino flux factor profiles. Bottom panel: RMS neutrino energy profiles.

neutrino luminosity per species L_{ν_i} at spherical radius r ,

$$L_{\nu_i}(r) = \oint d\omega \int d\varepsilon_\nu F_r(r, \varepsilon_\nu, \nu_i) r^2, \quad (11)$$

where F_r is the spectral radial neutrino flux in species ν_i at energy ε_ν . $d\omega$ is the spatial solid-angle element, $d\omega = 2\pi \sin\theta d\theta$ in axisymmetry. Furthermore, we define the mean inverse flux factor $\langle 1/F_{\nu_i} \rangle$,

$$\left\langle \frac{1}{F_{\nu_i}} \right\rangle = \frac{c \int d\varepsilon_\nu E(\varepsilon_\nu, \nu_i)}{\int d\varepsilon_\nu F_r(\varepsilon_\nu, \nu_i)}, \quad (12)$$

where $E(\varepsilon_\nu, \nu_i) = 4\pi c^{-1} J(\varepsilon_\nu, \nu_i)$ is the spectral neutrino energy density, and the neutrino RMS energies are

$$E_{\text{RMS}, \nu_i} = \sqrt{\frac{\int d\varepsilon_\nu \varepsilon_\nu^2 J(\varepsilon_\nu, \nu_i)}{\int d\varepsilon_\nu J(\varepsilon_\nu, \nu_i)}}. \quad (13)$$

The above three quantities are particularly useful diagnostics, since the ε_ν -averaged energy deposition rate by charged-

current absorption of ν_e and $\bar{\nu}_e$ on neutrons and protons scales linearly with their product (Messer et al. 1998).

4.3.1. Model s20.nr

In Fig. 7, we plot neutrino luminosities L_{ν_i} , angle-averaged mean inverse flux factors, and the angle-averaged E_{RMS} for the postbounce snapshot at 160 ms of the nonrotating model s20.nr. The asymptotic total luminosity at this time is $\sim 150 \text{ B s}^{-1}$ and is already dominated by the thermally-produced “ ν_μ ”s that cool the PNS, but contribute little to the heating in the gain region, since they cannot take part in charged-current absorption processes. In this quasi-spherically symmetric model, we define a spherical gain radius r_{gain} as the radial position beyond which net neutrino energy deposition occurs. At 160 ms after bounce, $r_{\text{gain}} \simeq 90 \text{ km}$ and the gain region extends almost out to the shock at $\sim 175 \text{ km}$. The MGFLD luminosities in Fig. 7 are systematically lower by $\sim 5\%$ for ν_e s, $\sim 3.5\%$ for $\bar{\nu}_e$ s, and $\sim 4\%$ for “ ν_μ ”s, but qualitatively resemble the S_n luminosity profiles in the gain region. At around the shock position, all MGFLD luminosities increase by $\sim 5\%$. This is due to the combination of the artificially spread-out shock (over ~ 4 – 5 zones), the rapid change of the inverse neutrino mean-free path in the spread-out shock and the implementation of the flux limiter in VULCAN/2D. Since this MGFLD artefact occurs right at the shock, it can have only little influence on the heating in the gain region, but leads to somewhat overestimated asymptotic luminosities in the MGFLD case.

The center panel of Fig. 7 shows the ε_ν -averaged inverse flux factors for the three neutrino species in the MGFLD and S_n steady-state calculations of model s20.nr. For isotropic radiation $\langle 1/F_{\nu_i} \rangle$ tends to infinity, while it approaches one when the radiation field becomes forward-peaked at low optical depth. Focussing on the gain region between r_{gain} and the shock position, we find that MGFLD yields mean inverse flux factors that are up to $\sim 5\%$ larger for $\bar{\nu}_e$ s (less for the other species) in the inner gain region. At radii $\gtrsim 150 \text{ km}$, the MGFLD $\langle 1/F_{\nu_i} \rangle$ quickly drops to 1 (free streaming), becoming up to 8% lower than the S_n values in the outer gain region. We note that “ ν_μ ” interact only via neutral-current weak interactions, hence, decouple from matter at higher densities and temperatures. Next in the decoupling hierarchy are electron anti-neutrinos followed by electron neutrinos. Both S_n and MGFLD realize this hierarchy at radii below $\sim 150 \text{ km}$, beyond which MGFLD rapidly transitions to free streaming irrespective of neutrino species.

The behavior we observe with radius of the luminosity and mean-inverse flux factor agrees with the general findings of Messer et al. (1998). In particular, we agree with their assessment that the artificially accelerated transition to free streaming in MGFLD occurs not at the neutrinospheres (which are generally below the gain region), but at relatively large radii within which most of the neutrino source is enclosed.

In the bottom panel of Fig. 7 we present profiles of the RMS neutrino energy for all species in MGFLD and S_n snapshots of model s20.nr. The corresponding luminosity spectra (extracted at 500 km) are shown in Fig. 8. Both MGFLD and S_n capture the energy systematics that is set essentially by the matter temperature in the decoupling region. Neutrino species that decouple at smaller radii (higher densities and tempera-

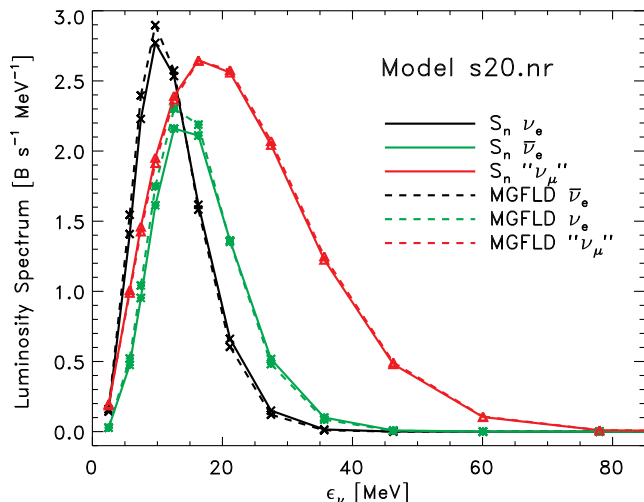


FIG. 8.— Neutrino luminosity spectra extracted at a radius of 500 km for ν_e , $\bar{\nu}_e$, and ν_μ neutrinos at 160 ms after bounce in model s20.nr. Solid lines correspond to S_n results, while dashed lines are obtained using MGFLD. The spectra have the canonical shape and the quantitative behavior found in nonrotating intermediate-time postbounce supernova calculations (e.g., Thompson et al. 2003) with the ν_μ -neutrinos peaking at the highest energies, since they decouple from the fluid at the smallest radii. MGFLD and S_n spectra agree closely in shape, but MGFLD is overestimating slightly the total asymptotic luminosity (cf. Fig 7).

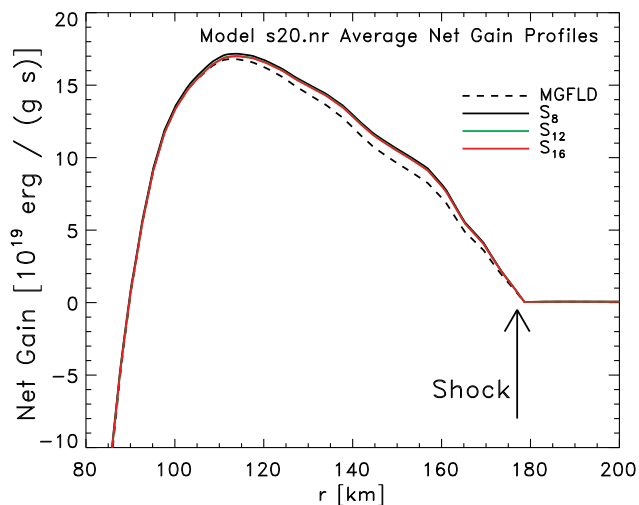


FIG. 9.— Angle-averaged specific neutrino net gain profile in the s20.nr model at 160 ms after core bounce. Shown are the MGFLD results, as well as results from steady-state S_n calculations with 8, 12, and 16 ϑ -angles, corresponding to a total number of angular zones of 40, 92, and 162. The gain region extends from ~ 90 km to the shock position at ~ 175 km. The three different S_n resolutions yield net gain profiles that agree very well (relative differences below 1% even for S_8). The MGFLD calculation underestimates the total net gain in the outer gain region by at most 10% locally and $\lesssim 5\%$ on average.

tures) have higher RMS energies and harder spectra than neutrinos decoupling at larger radii. Quantitative differences in RMS energies and in the spectra between MGFLD and S_n are small, the slightly higher MGFLD spectral luminosities being mostly a result of the artificially enhanced MGFLD luminosities near and beyond the shock.

We now conclude our discussion of the 160 ms-postbounce snapshot of model s20.nr by considering the instantaneous neutrino energy deposition rates. Figure 9 depicts angle-averaged radial profiles of the specific neutrino heating/cooling rates in units of erg (g s)^{-1} . The region of net gain

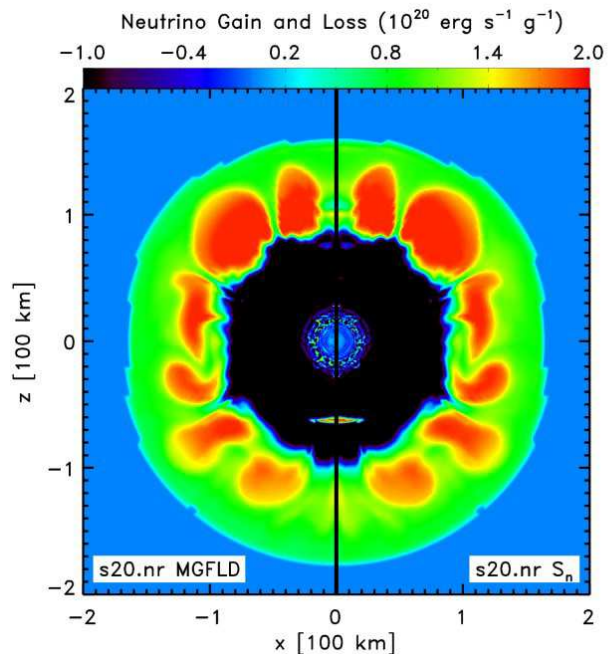


FIG. 10.— 2D colormap of the specific (per gram) net gain distribution in model s20.nr at 160 ms after core bounce. The left half of the plot depicts the MGFLD result, S_n is shown on the right. The differences between S_n and MGFLD are marginal at this time in this model and are practically indiscernible by eye. As a consequence of convection in the gain region and the onset of the SASI, even this nonrotating model exhibits significant angular and radial variations in the neutrino energy deposition not captured by the average profiles in Fig. 9.

extends from ~ 90 km to the shock radius and the chief contribution to the heating comes from charged-current $\bar{\nu}_e$ -capture processes on protons, exceeding the corresponding ν_e -capture on neutrons by a factor of two and more in the narrow radial interval from 145 to 175 km. MGFLD underestimates the specific net gain in the angle-averaged radial profile by at most 10% locally and by $\sim 5\%$ on average at radii greater than ~ 110 km. The integral total net gain predicted by S_{16} is 2.13 B s^{-1} . This is only 3% larger than the MGFLD value of 2.07 B s^{-1} . We note in passing that S_8 overestimates the integrated gain rate by at most $\sim 1.6\%$ while S_{12} agrees with S_{16} to better than $\sim 0.3\%$.

Figure 10 depicts the 2D distribution of neutrino heating and cooling in the snapshot of model s20.nr considered here. Regions of net gain range from green to red, cooling regions are blue to black. The colormap demonstrates the somewhat misleading character of angle-averaged profiles. While we find that there is little spatial angular variation in the neutrino radiation field, the neutrino-matter coupling depends strongly on angular position, and energy deposition is generally greatest in regions of high entropy (cf. Fig 2).

4.3.2. Model s20.π

As we discussed in the context of the Eddington tensor in §4.2 and as may be guessed from the significant rotational deformation of the core in model s20.π (Fig. 2), the radiation field in this model exhibits a strong rotationally-induced asymmetry between pole and equator. In Fig. 11, we present 2D colormaps of the radial spectral flux component (in $\text{erg s}^{-1} \text{cm}^{-2} \text{MeV}^{-1}$) and isoenergy-density contours ($4\pi J_\nu/c$ in $\text{erg cm}^{-3} \text{MeV}^{-1}$) at a representative ε_ν of 12.6 MeV and for

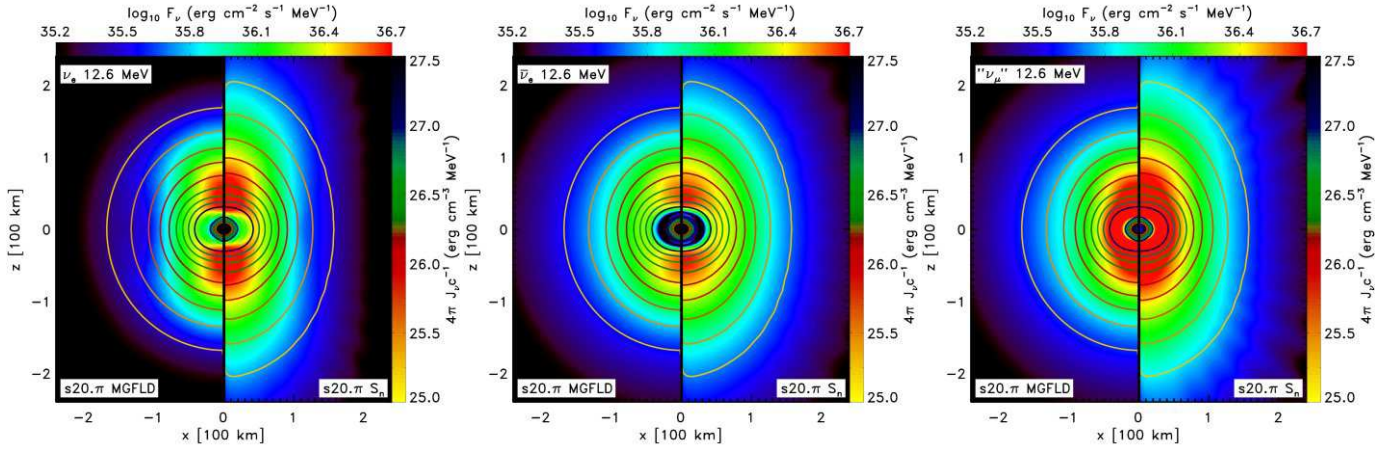


FIG. 11.— Colormaps of the radial spectral flux at $\varepsilon_\nu = 12.6$ MeV of ν_e (left), $\bar{\nu}_e$ (center), and “ ν_μ ” (right) neutrinos in the rapidly-rotating model s20. π at 160 ms after bounce. Isoenergy density contours ($4\pi c^{-1}J_\nu$, vertical color legend) are superposed. The left half of each panel displays the MGFLD result – S_n is shown in the right half. The radiation fields are oblate in the PNS core and deform to a prolate shape further out. Note that S_n predicts a prolateness of the radiation field to much greater radii than MGFLD does. The latter leads to nearly spherically symmetric radiation fields at radii greater than $\gtrsim 150$ –200 km independent of neutrino species.

all species. Numbers for both S_n and MGFLD are compared side by side. The global radiation-field anisotropy systematics are qualitatively similar to what was found in the previous MGFLD rotating core-collapse study of Walder et al. (2005). At small radii, the radiation field (energy density) follows the density distribution and is oblate, but in the snapshot at 160 ms after bounce shown in Fig. 11 has a pole–equator ratio of only 1:2. This ratio increases as the PNS cools and contracts. The polar compactness of the PNS core leads to a decoupling of matter and neutrinos at smaller radii in regions near the pole, resulting there in greater spectral fluxes at higher neutrino energies and in a prolate distribution of neutrino fluxes and isoenergy-density contours.

The most striking difference between the S_n and MGFLD radiation fields presented in Fig. 11 is the former’s much greater prolateness at large radii for all species (and all energies, though we show only $\varepsilon_\nu = 12.6$ MeV). With the MGFLD prescription, the prolateness of the flux is muted and does not extend to large radii. Though the radiation fields are smoothed out at radii $\gtrsim 150$ km by MGFLD, the S_n fluxes and energy densities remain prolate through the entire postshock region and beyond. At radii outside ~ 200 km, the typical striping pattern of S_n (Castor 2004) becomes visible, though not yet dominant.

In Fig. 12, we plot line profiles of the polar and equatorial “luminosities” ($4\pi r^2 F_r$) of each neutrino species. Profiles obtained with S_n and MGFLD are shown. The asymptotic “luminosities” obtained with S_n have pole-to-equator ratios of 2.2 (ν_e), 1.8 ($\bar{\nu}_e$), and 2.4 (“ ν_μ ”). MGFLD smoothes out these large asymmetries, yielding higher equatorial and significantly lower polar “luminosities” at radii greater than ~ 100 km. This is consistent with the more qualitative findings based on Fig. 11. We note that the MGFLD variant of VULCAN/2D still conserves total flux and energy. For the S_n calculation, we find total asymptotic luminosities of 21.1 B s^{-1} for ν_e neutrinos (MGFLD: 20.4 B s^{-1}), 22.7 B s^{-1} for $\bar{\nu}_e$ neutrinos (MGFLD: 22.6 B s^{-1}), and 53.0 B s^{-1} for “ ν_μ ” neutrinos (MGFLD: 52.3 B s^{-1}). Hence, S_n and MGFLD total luminosities per species agree very well (and differ at most by $\sim 3.5\%$ in the ν_e case), while their flux distributions disagree significantly.

Figure 13, depicting polar and equatorial “luminosity” spectra ($4\pi r^2 F_r(\varepsilon_\nu)$), reveals that in the S_n calculation (polar: black graphs, equatorial: red graphs) the neutrino radiation emerging from the PNS and postshock environments through the polar region not only has greater fluence, but also a significantly different and – in the ν_e case – a significantly harder spectrum. ν_e neutrinos decouple at the largest radii. Their “luminosity” spectrum observed by a polar observer peaks at $\varepsilon_\nu \sim 9.5$ MeV, while for an observer near the equator it peaks at ~ 7.5 MeV. Both $\bar{\nu}_e$ and “ ν_μ ” neutrinos (which decouple further in) exhibit a smaller variation in peak energy from pole to equator. The MGFLD calculation, on the other hand, shows much smaller variations in neutrino energy and flux between pole and equator (green and blue graphs, respectively). We note in passing that the emerging neutrino spectra of model s20. π are systematically softer by up to $\sim 10\%$ in each species than those of the nonrotating model s20.nr presented in Fig. 8. This is a direct consequence of the rotationally-induced lower overall compactness of the PNS in model s20. π .

The RMS neutrino energies in model s20. π show the same overall qualitative behavior and decoupling hierarchy discussed in the context of model s20.nr. Hence, we do not show them here, but rather state quantitative results. They do, of course, trace the strong pole–equator asymmetry that we observe in the radiation field. The RMS energies in the 160 ms S_n snapshot are 11.5 MeV (pole) and 10.5 MeV (equator) for ν_e , 16.7 MeV (pole) and 15.2 MeV (equator) for $\bar{\nu}_e$, and 25.8 MeV (pole) and 24.8 MeV (equator) for “ ν_μ ” neutrinos. The MGFLD values converge at pole and equator to 10.5 MeV (ν_e), 15.2 MeV ($\bar{\nu}_e$), and 25.0 MeV (“ ν_μ ”).

In Fig. 14, we plot polar and equatorial mean inverse flux factor profiles for ν_e and $\bar{\nu}_e$ neutrinos in our steady-state snapshot for model s20. π . Results from MGFLD and S_{16} runs are shown. A free-streaming radiation field has an inverse flux factor of one. Due to the steeper density gradient in polar regions, neutrinos decouple from matter at smaller radii than at the equator. While MGFLD must handle the decoupling and increased forward-peaking of the radiation field via the flux limiter, S_n can track it self-consistently. For ν_e neutrinos and along the poles, S_n predicts significantly greater mean inverse flux factors with shallower slopes than MGFLD, indicating a

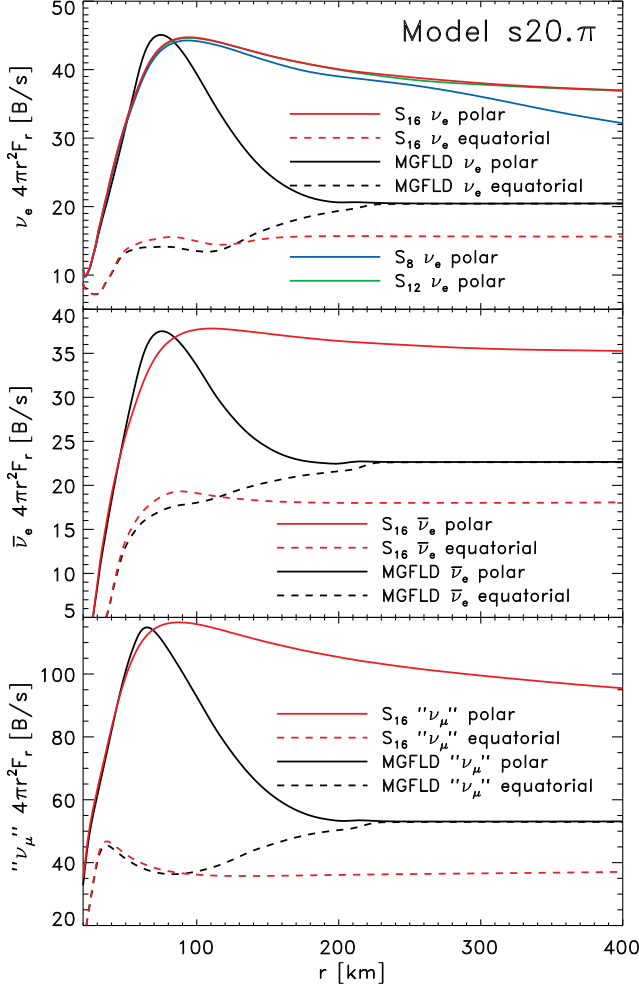


FIG. 12.— Radial neutrino “luminosity” profiles ($4\pi r^2 F_r$) as seen by observers near the pole (solid lines) and near the equator (dashed lines) in model $s20.\pi$ at 160 ms after bounce. Red graphs correspond to S_n results, black graphs depict MGFLD results. Top, center, and bottom panels show L_ν for ν_e , $\bar{\nu}_e$, and ν_μ , respectively. All S_n results were obtained with $n = 16$, but for comparison we also plot in the top panel polar profiles that were obtained with S_8 and S_{12} and find that both S_{16} and S_{12} are very well converged, while S_8 has troubles at radii greater than ~ 200 km. However, it agrees very well at smaller radii with the higher-resolution S_n calculations.

more gradual transition to free streaming than predicted by the flux limiter. In the radial interval of ~ 60 – 100 km, the relative difference is ~ 12 – 19% , decreasing to ~ 6 – 12% out to 200 km. In equatorial regions, the ν_e radiation field is somewhat more forward-peaked in the S_n calculation at radii below ~ 120 km, beyond which MGFLD transitions quickly to free streaming while S_n approaches it more gradually, exhibiting ~ 6 – 8% larger mean inverse flux factors in the outer postshock region. For $\bar{\nu}_e$ neutrinos, the behavior of the mean inverse flux factors in polar regions essentially mirrors that observed for the ν_e s. In equatorial regions, the S_n mean inverse flux factor of the $\bar{\nu}_e$ s stays below that using MGFLD out to 165 km, beyond which the MGFLD $\bar{\nu}_e$ radiation field rapidly transitions to free streaming. At 180 km, the MGFLD $\bar{\nu}_e$ mean inverse flux factor is $\sim 1\%$ smaller than that predicted by S_n . At 220 km, this difference has grown to $\sim 5\%$.

Having established the overall neutrino radiation-field characteristics in the 160-ms postbounce snapshot of model $s20.\pi$, we now turn our focus to the neutrino cooling and heating

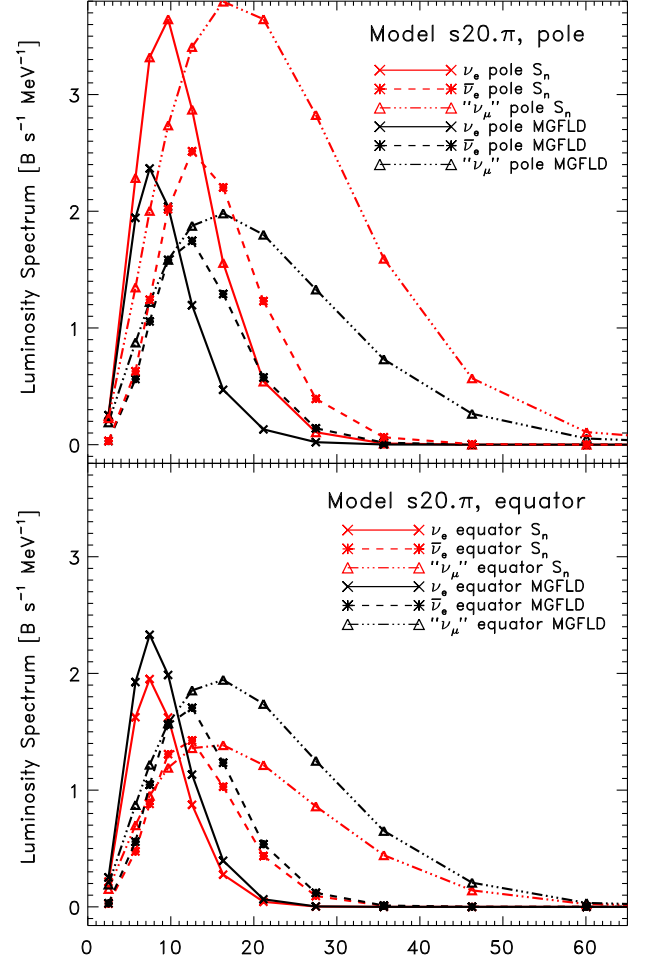


FIG. 13.— **Top:** Neutrino “luminosity” spectra ($4\pi r^2 F_r(\epsilon_\nu)$) in S_n (red) and MGFLD (black) variants of model $s20.\pi$ as seen by observers near the pole. ν_e spectra have solid lines, $\bar{\nu}_e$ spectra are shown in dashed lines, and ν_μ s have dash-dotted spectra. The spectra are taken from a S_{16} calculation at a radius of 300 km at 160 ms after core bounce. **Bottom:** “Luminosity” spectra seen by equatorial observers.

rates in this model. We have found little difference in the net neutrino heating between S_n and MGFLD variants in the 160-ms postbounce snapshot of the nonrotating model $s20.nr$. However, based on the differences between S_n and MGFLD in neutrino fluxes, RMS energies, and flux factors we have highlighted in this section, we may expect to find significant differences in the neutrino heating rates for model $s20.\pi$.

Figure 15 depicts 2D colormaps of the neutrino energy gain and loss rate per unit mass (accounting for all energies and species), computed for the 160-ms postbounce snapshot of model $s20.\pi$ using S_n (left panel) and MGFLD (right panel). At low latitudes near the equator, S_n and MGFLD agree very well to the eye. In regions near the pole, both MGFLD and S_n show a pronounced region of net loss at z -coordinates between ~ 40 and ~ 80 km, beyond which a region of net gain (colors light blue and green to red) prevails out to the shock position at ~ 230 km. While the gain region has roughly the same physical extent in MGFLD and S_n , the latter yields significantly higher energy deposition rates. This is particularly the case in the lower gain region at polar angles below $\sim 20^\circ$ and at radii between ~ 80 and 150 km, where the S_n gain rate is larger by a factor of two and more. The top panel in Fig. 16

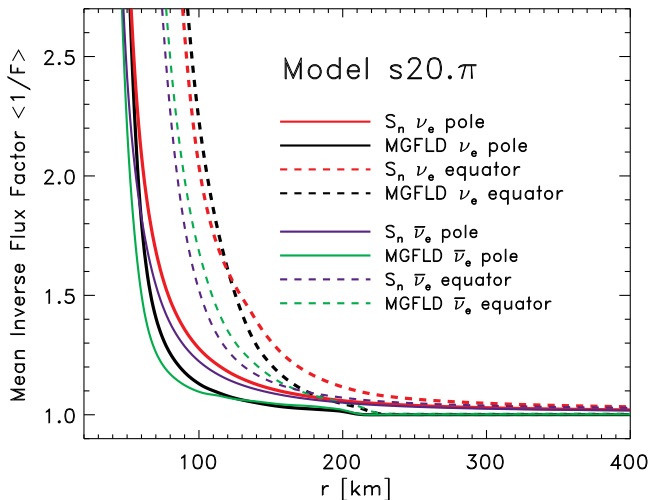


FIG. 14.— Mean inverse flux factors in model s20.π at 160 ms after bounce in polar regions (solid lines) and equatorial regions (dashed lines). Shown are profiles for ν_e neutrinos obtained with S_n (red) and MGFLD (black), as well as profiles for $\bar{\nu}_e$ neutrinos (S_n blue, MGFLD green). S_n and MGFLD graphs agree well inside ~ 50 km at the pole and inside ~ 80 km in equatorial regions. For ν_e neutrinos, S_n yields systematically larger mean inverse flux factors in polar and equatorial regions. For $\bar{\nu}_e$, however, S_n predicts larger mean inverse flux factors in polar regions, yet transitions slightly faster than MGFLD to free streaming in equatorial regions.

provides a more quantitative comparison of S_n and MGFLD gain/loss rates, since it contrasts average specific gain/loss profiles obtained from polar and equatorial 20° wedges. In the polar region, the S_n gain region begins at a radius of ~ 80 km (MGFLD: ~ 88 km) and the S_n specific gain rate magnitude exceeds the MGFLD numbers by a factor of 2.6 at 100 km, increasing to 3.2 at 200 km. Near the equator, net energy deposition occurs only in a small radial interval of ~ 90 – 120 km and the MGFLD specific gain rate is larger by 80% at 95 km, 41% at 100 km, and 26% at 110 km. The net energy loss between ~ 120 – 210 km (captured by both S_n and MGFLD) results from strong electron capture that dominates energy deposition by neutrino absorption.

The observed local differences in neutrino energy deposition between S_n and MGFLD are due primarily to the vastly different degree to which the two schemes capture the global pole-equator asymmetry of the radiation field in the rapidly-rotating postbounce supernova core of model s20.π. S_n yields much larger fluxes in the polar direction than MGFLD, but predicts lower neutrino fluxes in equatorial regions (cf. Fig. 12). Differences in the radial mean-inverse flux factors and RMS energies are much smaller, and, hence, are of only secondary importance. The S_n steady-state snapshot yields an integrated gain rate of 1.603 B s^{-1} while MGFLD predicts 1.637 B s^{-1} for the s20.π snapshot under consideration. This corresponds to $\sim 2.1\%$ more energy deposition per unit time in the MGFLD calculation. Given the above discussion, the reader may be surprised by these numbers. The explanation consists of two factors. Owing to rotation, the amount of mass per unit volume (i.e., the rest-mass density) is higher at any given equatorial radius than at the same radius in the polar direction. Plotting the neutrino gain/loss rate per unit volume instead of per unit gram, the bottom panel of Fig. 16 clearly shows the rotation-induced enhancement of the energy deposition (per unit volume) near the equator and the larger gain rate per unit volume predicted by MGFLD at small to intermediate radii. The second factor is the simple fact that the

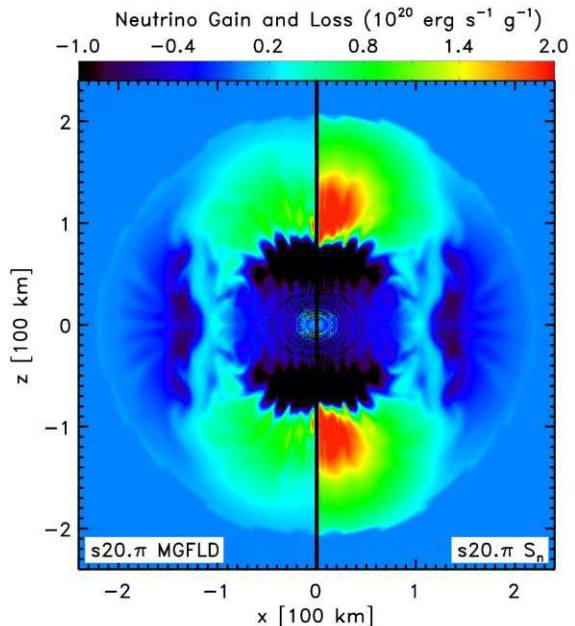


FIG. 15.— Colormaps of energy- and species-integrated specific neutrino energy deposition and loss rates in the rotating model s20.π at 160 ms after core bounce (in units of $\text{erg s}^{-1} \text{ g}^{-1}$). The left section of the plot depicts the MGFLD result and the right shows the result of the S_n calculation. Note the distinctively enlarged polar gain regions and greater specific gain of the S_n result compared to the MGFLD calculation. This is in part a consequence of the larger polar neutrino fluxes and overall greater flux asymmetry in the S_n model (see Fig. 11). A feature prevalent in both S_n and MGFLD versions of this rapidly rotating core is an extended loss region between the shock and the small gain region at low latitudes (cf. Fig. 16). The material in the loss region is still proton rich ($Y_e \gtrsim 0.4$) and efficiently captures electrons as it advects in, radiating away a significant flux of neutrinos (see, e.g., the increase in the equatorial “luminosity” between 120 and 150 km in the S_n variant of this model, visible in the top panel of Fig. 12). Note that both MGFLD and S_n exhibit a very small artefact (lower gain/loss) at the symmetry axis associated with imperfect numerics/regularization.

volume of the equatorial gain regions is much larger than that of the polar gain regions.

As we shall discuss in the following section, the large local differences in neutrino heating between the S_n and MGFLD snapshots have a dynamical consequence for the rapidly rotating model and lead to a significant polar expansion of the shock in the S_n postbounce evolution calculation.

5. RESULTS: EVOLUTION CALCULATIONS

In order to study differences between S_n and MGFLD in a time-dependent postbounce setting, we follow our relaxed 160-ms S_n models in fully coupled radiation-hydrodynamics fashion for ~ 340 ms (model s20.nr) and 390 ms (model s20.π) of postbounce time. In parallel with the S_n runs, we continue their MGFLD counterparts for the same time span.

5.1. Model s20.nr

Since we begin the MGFLD and S_n calculations from an identical hydrodynamic configuration at 160 ms after bounce, any qualitative or quantitative differences in their evolutions must ultimately be due to differences in the neutrino heating and cooling between S_n and MGFLD.

In the left panel of Fig. 17, we display the time evolution of the integral neutrino energy deposition (net gain) in

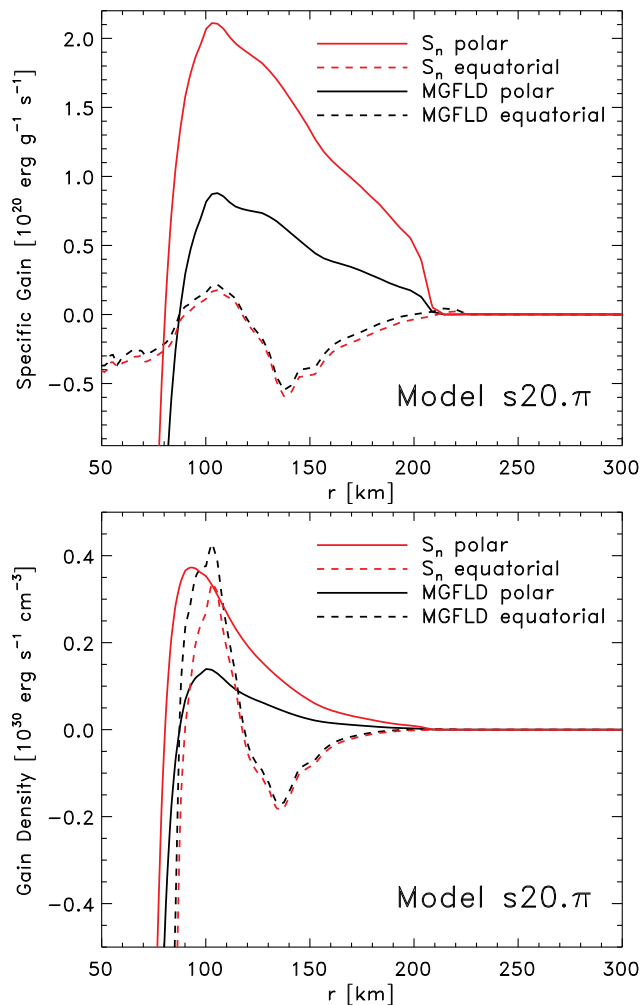


FIG. 16.— **Top:** Averaged specific radial neutrino gain and loss profiles in model $s20.\pi$ at 160 ms after core bounce. Shown are results from the S_n (red) and MGFLD (black) calculations. Both polar and equatorial radial profiles are obtained by averaging over 20° wedges. As is already clear from Fig. 15, S_n yields significantly greater polar specific neutrino energy gain than MGFLD. The S_n gain region extends further in by ~ 10 km and the gain is more than a factor of two larger in the interval from ~ 90 to 200 km. Given the larger flux asymmetry in the S_n calculation (Fig. 11), less neutrino flux is going through regions of low latitude, resulting in the *lower* specific gain at low latitudes predicted by S_n . **Bottom:** Neutrino gain density (density-weighted specific gain). Due to rapid rotation higher densities obtain out to larger radii at low latitudes. This results in a partial reversal of the picture presented by the upper panel; weighted by density, the neutrino gain (now per unit volume) in the equatorial wedge becomes comparable to that near the poles. Furthermore, equatorial regions, since they subtend the largest solid angles, contribute most to the volume integral. The integral numbers for the net gain in the polar wedge (counting both poles) for S_n (MGFLD) are 0.17 B s^{-1} (0.047 B s^{-1}) and in the equatorial wedge are 0.35 B s^{-1} (0.47 B s^{-1}). The total integrated net gain is 1.603 B s^{-1} and 1.637 B s^{-1} for S_n and MGFLD, respectively. These numbers are surprisingly close given the large qualitative and quantitative *local* differences in the neutrino gain distribution.

the gain region of model $s20.nr$. The net gain systematically declines at early postbounce times, due (a) to the declining neutrino luminosity and (b) to the rapid settling of accreting material into the net loss region near the PNS core (cf. Fig. 7 of Marek & Janka 2007). At later times, SASI-modulated convection increases the dwell time of accreting outer core material in the gain layer and the slope of the net gain evolution flattens. Both S_n and MGFLD track these systematics without qualitative difference. The S_n calculation predicts on average ~ 5 – 10% higher net gain in the postbounce interval

from ~ 160 ms to ~ 220 ms. Between ~ 220 ms and ~ 280 ms, MGFLD and S_n net gain rates agree to within a few percent. Towards the end of this interval, the net gain of the S_n calculation grows and settles at values that are on average 20–30% higher than those of the MGFLD run. This trend is confirmed by the right panel of Fig. 17, which portrays the heating efficiency, defined as the ratio of net gain to the sum of ν_e and $\bar{\nu}_e$ luminosities.

The left panel of Fig. 18 depicts the temporal evolution of the ν_e “luminosities” ($4\pi r^2 F_r$) as seen by observers situated at 250 km along the north pole and south pole as well as in the equatorial plane of models $s20.nr$ and $s20.\pi$. Here we focus on model $s20.nr$ and note for the S_n variant that north pole (thin solid black lines) and south pole (thin solid green lines) “luminosities” agree (on average) in magnitude, but exhibit oscillations about their temporal average that are roughly out of phase by half a cycle. The MGFLD calculation (thin dashed lines), on the other hand, does exhibit some short-period “luminosity” variations, yet shows no appreciable difference between poles and equator.

The time at which S_n begins to yield systematically larger neutrino heating rates (Fig. 17) coincides with the growth of the SASI-related shock excursions to large amplitudes (Fig. 19). This suggests that the increased heating is related at least in part to the S_n variant’s ability to better capture radiation field asymmetries (see also the discussion in §4.3.2), induced at late times by the rapidly varying shock and post-shock hydrodynamics in this model. Other factors that contribute to the increased heating in the S_n calculation are the higher RMS neutrino energies (by $\sim 5\%$; shown in the right panel of Fig. 18) and the more gradual transition of the S_n neutrino radiation field to free streaming in the postshock region (see §4.3.1).

Figure 20 contrasts S_n and MGFLD simulations of model $s20.nr$ by means of colormaps depicting the specific entropy distributions in the two variants. To visualize the hydrodynamic flow, we superpose fluid velocity vectors. Each panel of this figure corresponds to a specific postbounce time and each panel’s left-hand-side depicts the state of the MGFLD calculation, while the right-hand-side depicts the corresponding S_n calculation. The figure covers a postbounce interval from 160 ms (top left) to 500 ms (bottom right). At the beginning of the runs, the SASI-driven deviation from sphericity of the stalled shock is mild, but grows with time, showing $\ell = 1$ excursions now generally recognized as characteristic of the SASI¹⁰ (Scheck et al. 2008; Marek & Janka 2007; Bruenn et al. 2006; Burrows et al. 2007c).

As expected from the discussion of the $s20.nr$ 160-ms postbounce steady-state snapshot in §4, S_n and MGFLD variants of this model do not differ significantly in the early SASI phase. However, at later SASI stages, in particular at postbounce times $\gtrsim 300$ – 350 ms, the simulations diverge, showing different local qualitative and quantitative behavior within the overall SASI theme. This is also reflected in Fig. 19,

¹⁰ At least in detailed 2D models. Iwakami et al. (2008) carried out an exploratory 3D numerical study with nonrotating progenitors that suggests that in the 3D case the $\ell=1$ dominance still obtains, yet reaches smaller relative amplitudes, since not only higher ℓ modes, but also m modes, may now contain power. However, Yamasaki & Foglizzo (2008), who performed a perturbative study without symmetry constraints, argued that in the 3D case with rotation, a dominant $m = 1$ ($m = 2$) mode is likely to emerge in the case of slow (rapid) rotation.

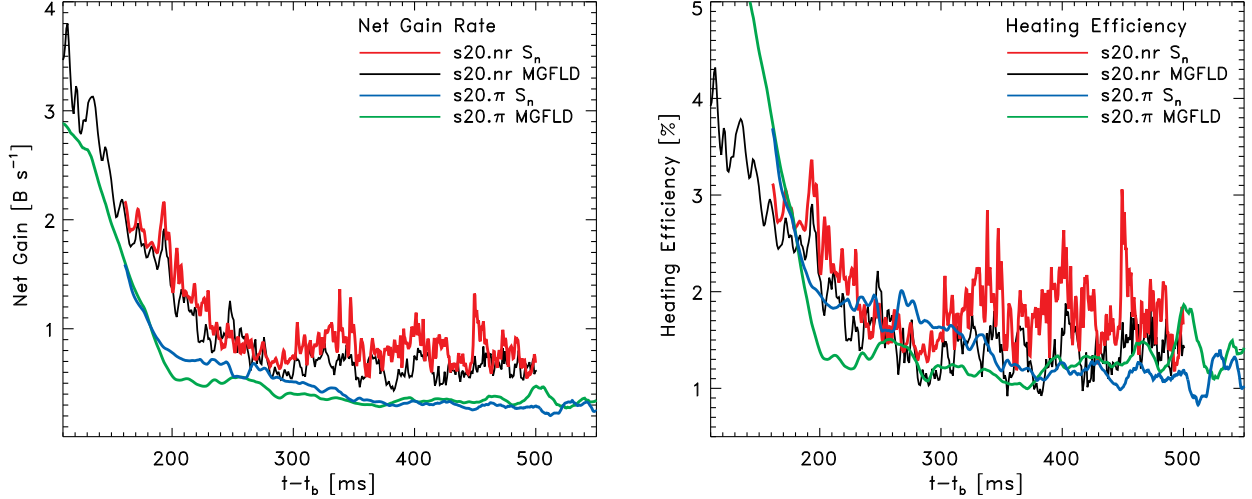


FIG. 17.— **Left:** Evolution of the total neutrino net gain rate as a function of postbounce time in the S_n and MGFLD variants of models $s20.nr$ and $s20.\pi$. At postbounce times before ~ 300 ms in model $s20.nr$, S_n yields a net gain rate that is larger by (on average) ~ 10 – 15% than that predicted by MGFLD. As the SASI becomes more pronounced at postbounce times $\gtrsim 300$ ms, the S_n net gain begins to more significantly exceed that of MGFLD, averaging out at ~ 20 – 30% larger values than the MGFLD net gain rate. In model $s20.\pi$, S_n and MGFLD net gain rates stay very close in the first ~ 30 ms of evolution, yet depart when the S_n variant approaches its new dynamical equilibrium (see Fig. 19) and provides for a larger gain region (mass and volume). This leads to a net gain rate that is larger by ~ 20 – 25% (on average in the postbounce interval from 200–350 ms). At later times, the MGFLD calculation, approaching the S_n variant’s postshock extent (Fig. 19) produces larger net gain rates due to its larger equatorial neutrino fluxes at similar hydrodynamic configuration. **Right:** Heating efficiency evolution in the two models with their S_n and MGFLD variants. We define the heating efficiency as the ratio of total neutrino net gain rate and the sum of electron and anti-electron neutrino luminosities.

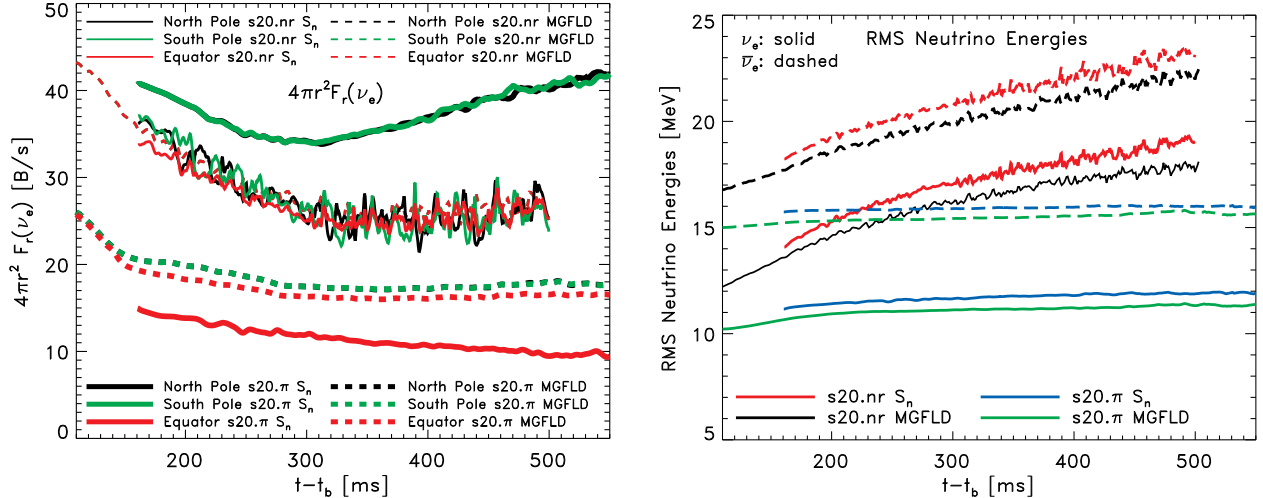


FIG. 18.— **Left:** ν_e “luminosities” ($4\pi r^2 F_r$) as a function of postbounce time as seen by observers located at a spherical radius of 250 km along the north pole (black lines), south pole (green lines), and in the equatorial plane (red lines) in S_n (solid lines) and MGFLD (dashed lines) variants of model $s20.nr$ (thin lines) and $s20.\pi$ (thick lines). Note that the south pole, north pole, and equator MGFLD “luminosities” in model $s20.nr$ (thin dashed lines) are very similar. Their lines are indistinguishable. The same holds for the south and north pole MGFLD “luminosities” in model $s20.\pi$ (thick black and green dashed lines). **Right:** Angle-averaged RMS energies of ν_e (solid lines) and $\bar{\nu}_e$ (dashed lines) neutrinos as a function of postbounce time in the S_n and MGFLD simulations the two models. S_n predicts systematically higher RMS neutrino energies in both models.

which depicts the evolution of the average shock radius, as well as the shock radii along north pole and south pole. The shock positions in the S_n and MGFLD simulations remain close and the SASI stays practically in phase (right panel of Fig. 19) until ~ 350 ms after bounce. Only then do they begin to show significant departures from each other. The SASI in the S_n calculation appears more pronounced at later times, exhibiting larger local (in time) shock excursions. Yet, quite surprisingly, given the significant increase in neutrino energy deposition, the S_n calculation does not exhibit any increase in the average shock radius, nor does it appear to be any closer to explosion than its MGFLD counterpart.

5.2. Model $s20.\pi$

The diagnosis of the radiation-hydrodynamic evolution of the rapidly spinning model $s20.\pi$ is less straightforward than for the nonrotating model $s20.nr$. As discussed in §4.3.2, rotation creates a global pole-equator asymmetry in the hydrodynamics of this model. MGFLD and S_n track the effect of globally asymmetric matter distributions on the neutrino radiation field to different degrees. In the steady-state snapshot at 160 ms, S_n predicts stronger neutrino heating in polar regions, yet weaker heating in the higher-density, larger-volume equatorial regions.

The polar, equatorial, and angle-averaged shock positions

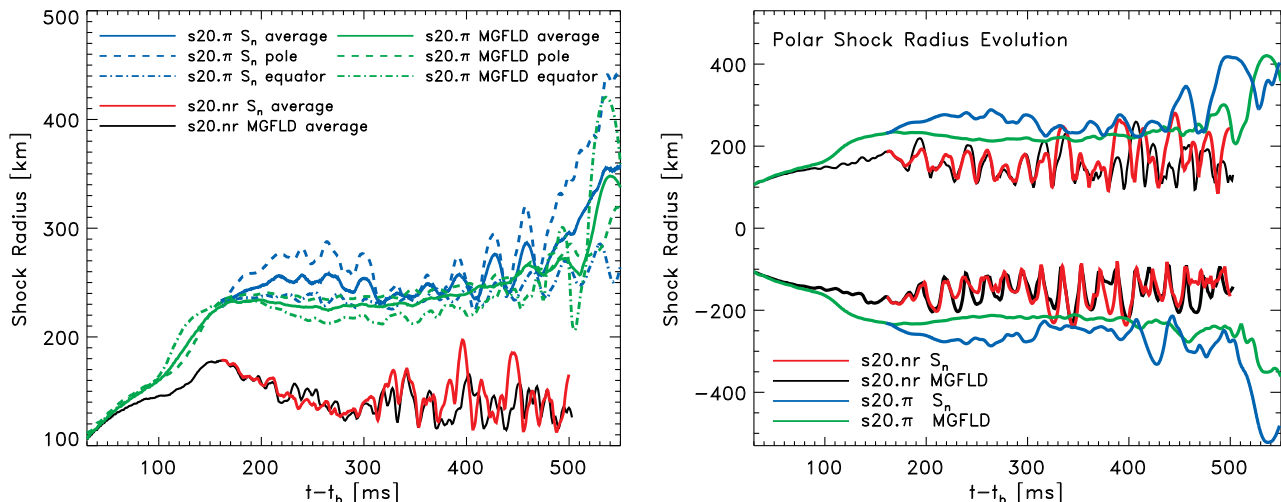


FIG. 19.— **Left:** Average shock radii as a function of postbounce time in S_n (red) and MGFLD (black) variants of the nonrotating model $s20.nr$. Also shown are the overall average shock radius, the average of south-pole and north-pole shock radii, and the equatorial shock radius for the rapidly spinning model $s20.\pi$, again for S_n (blue) and MGFLD (green). In model $s20.nr$, MGFLD and S_n show little quantitative deviation from each other. In the $s20.\pi$ evolution, however, a significant increase in the various shock radii is noticeable right at the beginning of the time-dependent S_n calculation. At later times MGFLD catches up and the average shock radii approach each other. The S_n variant exhibits larger variations, indicating stronger SASI-like shock excursions. **Right:** Evolution of the north-pole (positive) and south-pole (negative) shock radii for the S_n and MGFLD variants of the two models. Since the lowest-order and dominant mode of the 2D SASI is the $\ell=1$ polar sloshing mode, the polar shock radii are good indicators of its strength and periodicity. Note the initial suppression, but late-time development of SASI-like polar shock excursions in the rotating model.

portrayed by Fig. 19 show that the hydrodynamics responds immediately to the increased polar heating in the S_n calculation by a pronounced expansion of the shock along the poles. This expansion lasts for ~ 40 ms, after which the shock has expanded by $\sim 20\%$ from ~ 230 km to ~ 275 km on both poles. It stagnates at this radius and subsequently contracts again when feedback of the hydrodynamics to the neutrino microphysics leads to increased cooling (cf. the increased polar neutrino emission shown in Fig. 18). The increased postshock volume also results in a larger gain region and increased (compared to MGFLD) total neutrino energy deposition and heating efficiency. However, this increased heating is not able to sustain the large postshock volume. The shock slowly recontracts in the postbounce interval from ~ 250 ms to ~ 380 ms and eventually settles at radii similar to those obtained by the MGFLD shock.

In Fig. 21, we present a sequence of 2D entropy colormaps with superposed velocity vectors, portraying the postbounce evolution of model $s20.\pi$ from 160 ms on. The rapid rotation in this model not only partially stabilizes convection, but also weakens and delays the growth of the characteristic $\ell = 1$ SASI¹¹. Since larger shock radii are associated with an increased growth rate of the SASI (e.g., Fogliizzo et al. 2007; Scheck et al. 2008), the S_n variant begins to develop periodic shock excursions along the symmetry axis at much earlier times than the MGFLD simulation (Fig. 19). However, at times later than ~ 400 ms, the MGFLD model picks up the large-amplitude SASI as well and both calculations exhibit large-scale radial shock excursions beyond ~ 400 km along the pole (Fig. 19). The average shock radius increases in both calculations in this late postbounce phase. We observe neither such large shock excursions nor a systematic late-time increase of the average shock radius in the nonrotating model. The observed behavior is most likely due to the rapid rotation and the resulting rarefaction of the polar regions that reduces,

¹¹ But see the work of Yamasaki & Fogliizzo (2008), who find via perturbative analysis that in 3D, rotation enhances the development of azimuthal $m = 1$ and $m = 2$ SASI-related spiral structure.

in particular at late times, the ram pressure of accretion and allows for the more pronounced SASI.

In the left panel of Fig. 18, we contrast the ν_e “luminosities” ($4\pi r^2 F_r$) seen by observers located at a radius of 250 km above the north pole, the south pole, and in the equatorial plane of model $s20.\pi$. The MGFLD variant predicts a pole-equator flux asymmetry of $\lesssim 10\%$ that is roughly constant with time. The S_n calculation yields a very different picture. Polar and equatorial “luminosities” at 250 km (i.e., near the shock) are vastly different (cf. §4.3.2). Over time, the equatorial “luminosity” decreases while the “luminosity” along the poles is enhanced. At ~ 200 ms, polar and equatorial “luminosities” differ by a factor of ~ 3 . By ~ 500 ms, this factor has grown to 4. In addition, the S_n simulation shows SASI-induced variations in north and south-pole “luminosities” that grow to ~ 3 – 5% at late times and are not tracked in the MGFLD variant. These variations are akin those reported for the nonrotating model $s20.nr$, yet have longer periods, since the large shock excursions in model $s20.\pi$ occur on longer timescales.

As in the nonrotating model, we also find in model $s20.\pi$ that S_n yields systematically higher RMS neutrino energies for all species and at all times. However, as shown in the right panel of Fig. 18, the angle-averaged RMS energies do not exhibit a significant increase in the time interval covered by our simulations. This, again, is due to rapid rotation which slows down the PNS’s contraction. Not shown in Fig. 18, but present in the S_n variant throughout its postbounce evolution, are ~ 10 – 20% (roughly constant in time and independent of species) higher RMS energies for neutrinos emitted from polar regions compared to those emitted from the PNS equator. This is consistent with our analysis of the neutrino spectra and RMS neutrino energies for the 160 ms postbounce steady-state snapshot presented in §4.3.2.

We end our postbounce simulations of model $s20.\pi$ with S_n and MGFLD at 550 ms after bounce. Though within roughly the same qualitative picture, the two approaches to neutrino transport yield appreciable differences in the postbounce

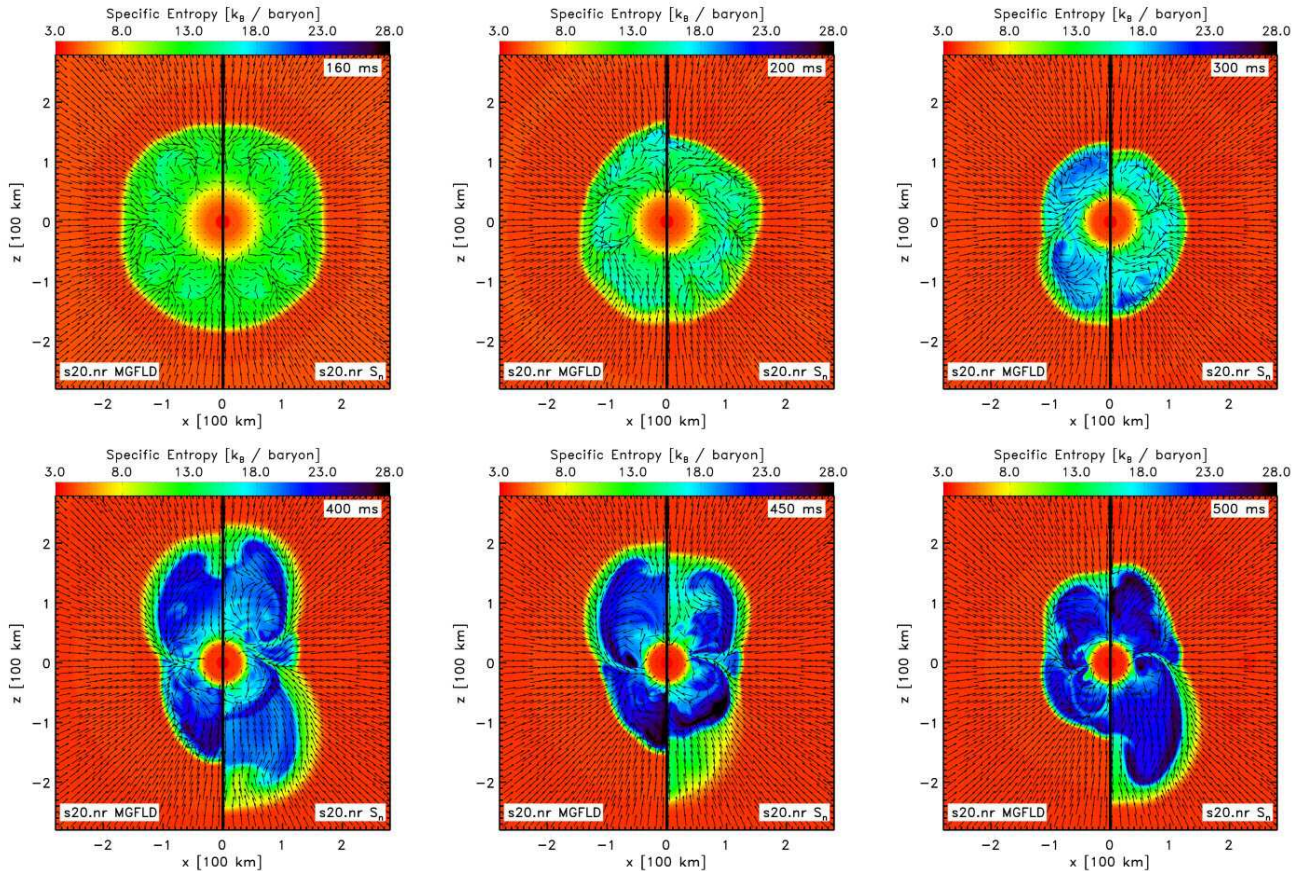


FIG. 20.— 2D entropy colormaps portraying the postbounce evolution of model s20.nr between 160 ms (top-left panel) and 500 ms (bottom-right panel) after core bounce. Fluid-velocity vectors are superposed to provide an impression of the flow. Each panel’s left-hand side corresponds to the MGFLD calculation and each panel’s right-hand side shows the S_n result. The time of each panel is given relative to the time of core bounce. The sequence of panels portrays the canonical development of the SASI in the nonrotating axisymmetric context. S_n and MGFLD evolution agree very well in the early SASI phases, but deviate in detail at later times, while still exhibiting the same overall SASI dynamics.

radiation-hydrodynamics evolutions. Importantly, and in contrast to our findings for the nonrotating model, S_n in model s20. π does not lead to systematically higher integral neutrino energy deposition, and at late postbounce times, shows a volume-integrated heating rate that is even $\sim 30\%$ lower (on average) than in its MGFLD counterpart.

6. SUMMARY AND DISCUSSION

Using the code VULCAN/2D (Livne et al. 2004; Burrows et al. 2007c; Livne et al. 2007), we perform long-term full-2D multi-angle, multi-group neutrino radiation-hydrodynamic calculations in the core-collapse supernova context. Based on postbounce hydrodynamic configurations from MGFLD simulations, we first compute 2D angle-dependent (S_n) steady-state solutions for models without precollapse rotation and with rapid rotation ($\Omega_0 = \pi \text{ rad s}^{-1}$). From these snapshots, we numerically follow the radiation-hydrodynamics evolution with S_n neutrino transport, tracking the nonrotating model to 500 ms and the rotating model to 550 ms after bounce.

Done for the first time in 2D, we investigate in detail the angle-dependent specific intensities and neutrino radiation fields. We compute angular moments of the specific intensity, including the Eddington tensor, and introduce Hammer-type map projections to visualize the angle dependence of the specific intensity. These we employ to demonstrate the decou-

pling systematics of the neutrinos and the gradual transition to free-streaming of the radiation fields with decreasing optical depth.

We compare our S_n simulations with MGFLD counterparts. We find for both models and at all times that the S_n specific intensity distributions transition less rapidly from isotropy to free-streaming in the semi-transparent outer postshock regions. S_n yields mean inverse flux factors and RMS neutrino energies in these regions that are $\sim 10\%$ larger than those obtained with MGFLD. In the context of the neutrino mechanism of core-collapse supernova explosions, differences in the net neutrino energy deposition rates between MGFLD and multi-angle S_n transport are of greatest interest. In the quasi-spherical early postbounce phase of the nonrotating model, we find that S_n predicts a 5–10% greater neutrino energy deposition rate than MGFLD. At later times, when the SASI has reached large amplitudes and globally deforms the postshock region, we find that S_n yields consistently larger (up to 30% on average) energy depositions and leads to significantly larger temporary shock excursions around average shock radii that do not depart much from those in the MGFLD calculation.

Convection on small and intermediate scales and SASI on large scales, are the key agents of the breaking of spherical symmetry in nonrotating (or slowly rotating) core-collapse supernovae. While we observe no large qualitative differences in the growth and dynamical evolutions of convection and SASI between nonrotating S_n and MGFLD models, we

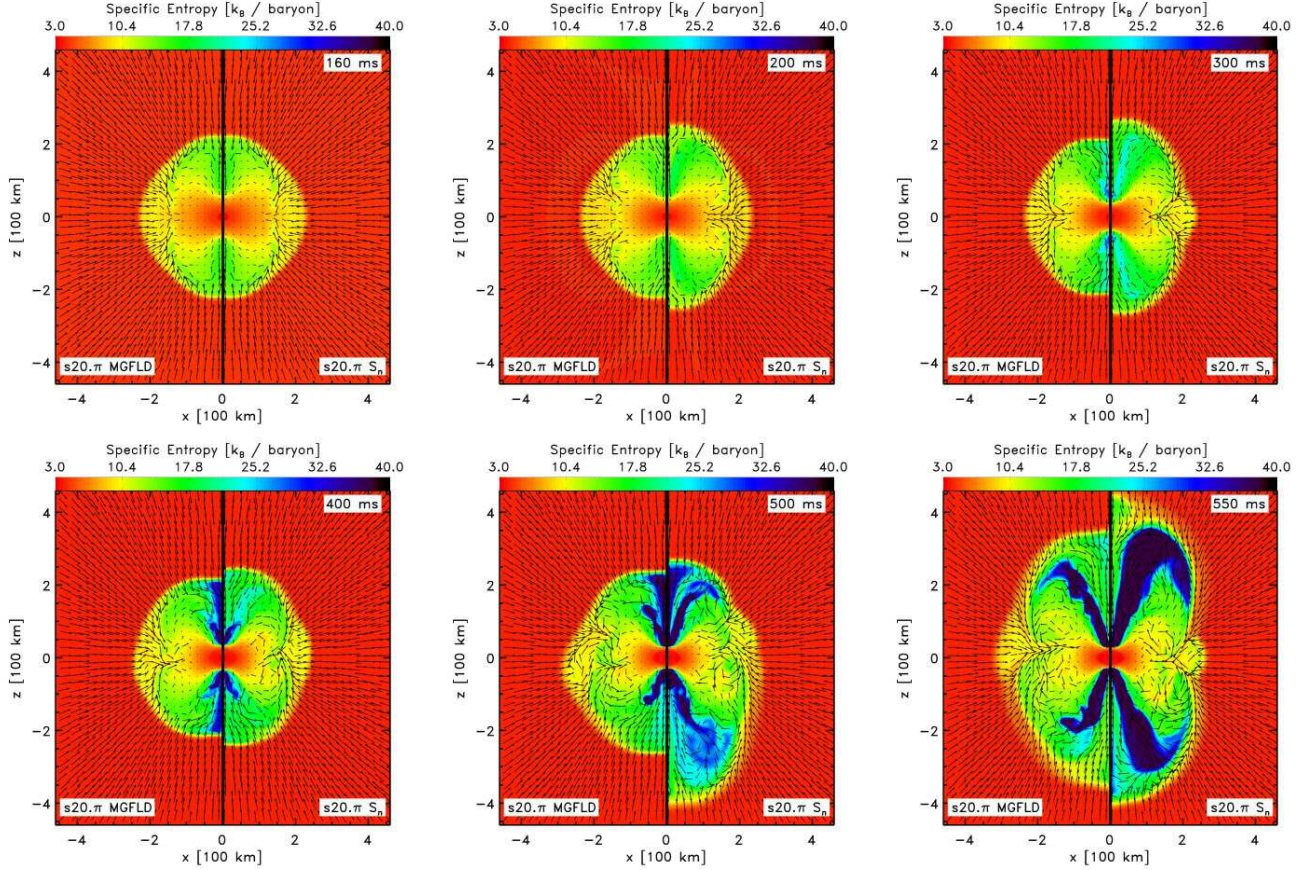


FIG. 21.— 2D entropy colormaps portraying the postbounce evolution of the rapidly-rotating model $s_{20,\pi}$ between 160 ms (top-left panel) and 550 ms (bottom-right panel) after core bounce. Fluid-velocity vectors are superposed to relay an impression of the flow and convey the partial suppression of convective overturn in regions of positive specific angular momentum gradient. As in Fig. 20, we plot the MGFLD result on the left-hand side and the S_n result on the right-hand side of each panel. Easily discernible is the immediate increase in the polar shock radius in the S_n calculation. This is a direct consequence of the increased polar neutrino heating in this variant (Figs. 15 and 16). At intermediate times, S_n and MGFLD shock positions grow closer, but later on in the postbounce evolution, the S_n variant begins to develop larger top-bottom SASI-like asymmetry and polar shock excursions at earlier time than its MGFLD counterpart.

find that the imprint of the asymmetric hydrodynamics on the neutrino radiation fields is captured with greater detail by the multi-angle transport scheme. For the late-time, heavily SASI-distorted postbounce core, S_n predicts asymptotic neutrino fluxes that have variations with time and angle of 5–10% in magnitude. MGFLD is able to capture the temporal variations of the neutrino luminosity, but smoothes out the angular flux variations at large radii/low optical depths.

Rapid rotation leads to large deviations from spherical symmetry and a rotationally-deformed PNS emits, by von Zeipel’s law of gravity darkening, a greater neutrino flux along its rotational axis than through its equatorial regions (Janka & Moenchmeyer 1989a,b; Kotake et al. 2003; Walder et al. 2005; Buras et al. 2006a; Dessart et al. 2006b). We find that both 2D MGFLD and S_n yield similar radiation fields and pole-equator flux ratios at radii smaller than ~ 100 km. At larger radii, the MGFLD radiation fields spheritize and show little pole-equator asymmetry in their asymptotic variables. S_n , on the other hand, captures large pole-equator flux ratios of up to 4:1 at late times and predicts polar neutrino spectra that are harder in peak energy (RMS energy) than on the equator by up to 30% (10–15%) for ν_e neutrinos, and somewhat less for the other species. All this results in a neutrino energy deposition rate per unit mass in polar regions that is locally up to ~ 2.5 –3 times higher when multi-angle transport is used. This increased polar neutrino heating has

a dynamical effect on the postbounce evolution, leading to rapid shock expansion in the polar regions and an earlier onset of the (initially) rotationally-weakened SASI. However, at late times, the SASI in the MGFLD calculation catches up and yields shock excursions of a similar magnitude.

In summary, our results show that 2D multi-angle neutrino transport manifests interesting differences with 2D MGFLD when addressing local and global radiation field asymmetries associated with rapid rotation and the non-linear SASI at late postbounce times. In addition, multi-angle transport results in enhanced neutrino energy deposition. The latter is most significant in the polar regions of rapidly rotating postbounce configurations and affects dynamically the postbounce evolution, including the growth of the SASI. However, in the large postbounce interval covered by our simulations, the local and global differences between multi-angle transport and MGFLD calculations do not appear large enough to alter the overall simulation outcome. Importantly, the multi-angle models do not appear to be closer to explosion than their MGFLD counterparts.

Although we neglect velocity-dependent transport terms and coupling of neutrino energy bins, we do not expect our conclusions to be altered by their inclusion, since they are not likely to affect significantly the differences between multi-angle transport and MGFLD. Further significant limitations of our present study are the neglect of general relativistic and

MHD effects, the restriction to only one finite-temperature nuclear EOS, the limited resolution in momentum-space imposed by the computational cost of multi-angle calculations, and the use of two spatial dimensions, plus rotation. In the future, we will investigate the dependence of our results (e.g., heating rates, radiation-field asymmetries etc.) on the choice of flux limiter and will consider different progenitor models.

The core-collapse supernova problem is one of many feedbacks. Larger heating rates and heating efficiencies than found in our models appear to be necessary to break the feedback cycle between neutrino radiation fields and hydrodynamics, revive the stalled shock, and unbind the supernova envelope – if the neutrino mechanism is to obtain in the way presently envisioned. Future work will have to go beyond the limitation of axisymmetry and must address in detail the entire ensemble of possible factors relevant in the supernova problem, including, but not limited to, 3D dynamics, multi-angle neutrino transport with velocity dependence and inelastic ν_e - e^- scattering, progenitor structure, rotational configuration, magnetohydrodynamics, convection, the SASI, PNS g-modes, general relativity, the nuclear EOS, and neutrino-matter interactions.

ACKNOWLEDGEMENTS

REFERENCES

- Adams, M. L., & Larsen, E. W. 2002, *Prog. Nuc. En.*, 40, 3
Akiyama, S., Wheeler, J. C., Meier, D. L., & Lichtenstadt, I. 2003, *ApJ*, 584, 954
Arnett, W. D. 1966, *Canadian Journal of Physics*, 44, 2553
Balbus, S. A., & Hawley, J. F. 1991, *ApJ*, 376, 214
Baron, E., Myra, E. S., Cooperstein, J., & van den Horn, L. J. 1989, *ApJ*, 339, 978
Bethe, H. A. 1990, *Rev. Mod. Phys.*, 62, 801
Bethe, H. A., & Wilson, J. R. 1985, *ApJ*, 295, 14
Blondin, J. M., Mezzacappa, A., & DeMarino, C. 2003, *ApJ*, 584, 971
Bowers, R. L., & Wilson, J. R. 1982, *ApJS*, 50, 115
Bruenn, S. W. 1985, *ApJS*, 58, 771
Bruenn, S. W., Dirk, C. J., Mezzacappa, A., Hayes, J. C., Blondin, J. M., Hix, W. R., & Messer, O. E. B. 2006, *J. Phys. Conf. Ser.*, 46, 393
Buras, R., Janka, H.-T., Rampp, M., & Kifonidis, K. 2006a, *A&A*, 457, 281
Buras, R., Rampp, M., Janka, H.-T., & Kifonidis, K. 2006b, *A&A*, 447, 1049
Burrows, A., Dessart, L., & Livne, E. 2007a, in *AIP Conference Series*, ed. S. Immler & R. McCray, Vol. 937, 370
Burrows, A., Dessart, L., Livne, E., Ott, C. D., & Murphy, J. 2007b, *ApJ*, 664, 416
Burrows, A., & Goshy, J. 1993, *ApJ*, 416, L75
Burrows, A., Hayes, J., & Fryxell, B. A. 1995, *ApJ*, 450, 830
Burrows, A., Livne, E., Dessart, L., Ott, C. D., & Murphy, J. 2006, *ApJ*, 640, 878
— 2007c, *ApJ*, 655, 416
Burrows, A., Young, T., Pinto, P., Eastman, R., & Thompson, T. A. 2000, *ApJ*, 539, 865
Castor, J. I. 1972, *ApJ*, 178, 779
— 2004, *Radiation Hydrodynamics (Radiation Hydrodynamics, by John I. Castor, pp. 368. ISBN 0521833094. Cambridge, UK: Cambridge University Press, November 2004.)*
Colgate, S. A., & White, R. H. 1966, *ApJ*, 143, 626
Cooperstein, J., & Baron, E. 1992, *ApJ*, 398, 531
Dessart, L., Burrows, A., Livne, E., & Ott, C. D. 2006a, *ApJ*, 645, 534
— 2007, *ApJ*, 669, 585
— 2008, *ApJ*, 673, L43
Dessart, L., Burrows, A., Ott, C. D., Livne, E., Yoon, S.-Y., & Langer, N. 2006b, *ApJ*, 644, 1063
Foglizzo, T., Galletti, P., Scheck, L., & Janka, H.-T. 2007, *ApJ*, 654, 1006
Foglizzo, T., & Tagger, M. 2000, *A&A*, 363, 174
Fryer, C. L., & Heger, A. 2000, *ApJ*, 541, 1033
Fryer, C. L., & Warren, M. S. 2002, *ApJ*, 574, L65
— 2004, *ApJ*, 601, 391
Hammer, E. 1892, *Petermanns Mitt.*, 38, 85
Heger, A., Langer, N., & Woosley, S. E. 2000, *ApJ*, 528, 368
Heger, A., Woosley, S. E., & Spruit, H. C. 2005, *ApJ*, 626, 350
Herant, M., Benz, W., Hix, W. R., Fryer, C. L., & Colgate, S. A. 1994, *ApJ*, 435, 339
Hubeny, I., & Burrows, A. 2007, *ApJ*, 659, 1458
Iwakami, W., Kotake, K., Ohnishi, N., Yamada, S., & Sawada, K. 2008, *ApJ*, 678, 1207
Janka, H.-T. 1992, *A&A*, 256, 452
— 2001, *A&A*, 368, 527
Janka, H.-T., Langanke, K., Marek, A., Martínez-Pinedo, G., & Müller, B. 2007, *Phys. Rep.*, 442, 38
Janka, H.-T., & Moenchmeyer, R. 1989a, *A&A*, 209, L5
— 1989b, *A&A*, 226, 69
Janka, H.-T., & Müller, E. 1996, *A&A*, 306, 167
Kitaura, F. S., Janka, H.-T., & Hillebrandt, W. 2006, *A&A*, 450, 345
Kotake, K., Yamada, S., & Sato, K. 2003, *ApJ*, 595, 304
Lattimer, J. M., & Prakash, M. 2007, *Phys. Rep.*, 442, 109
Lattimer, J. M., & Swesty, F. D. 1991, *Nucl. Phys. A*, 535, 331
LeBlanc, J. M., & Wilson, J. R. 1970, *ApJ*, 161, 541
Liebendörfer, M., Mezzacappa, A., Thielemann, F., Messer, O. E., Hix, W. R., & Bruenn, S. W. 2001, *Phys. Rev. D*, 63, 103004
Liebendörfer, M., Messer, O. E. B., Mezzacappa, A., Bruenn, S. W., Cardall, C. Y., & Thielemann, F.-K. 2004, *ApJS*, 150, 263
Liebendörfer, M., Rampp, M., Janka, H.-T., & Mezzacappa, A. 2005, *ApJ*, 620, 840
Livne, E. 1993, *ApJ*, 412, 634
Livne, E., Burrows, A., Walder, R., Lichtenstadt, I., & Thompson, T. A. 2004, *ApJ*, 609, 277
Livne, E., Dessart, L., Burrows, A., & Meakin, C. A. 2007, *ApJS*, 170, 187
Marek, A., & Janka, H.-T. 2007, Submitted to *ApJ*. ArXiv e-prints, 0708.3372 [astro-ph]
Messer, O. E. B., Mezzacappa, A., Bruenn, S. W., & Guidry, M. W. 1998, *ApJ*, 507, 353
Mezzacappa, A., & Bruenn, S. W. 1993a, *ApJ*, 405, 669
— 1993b, *ApJ*, 405, 637
Mezzacappa, A., & Messer, B. 1999, *J. Comp. Appl. Math.*, 109, 281
Mihalas, D., & Mihalas, B. 1984, *Foundations of Radiation Hydrodynamics (Mineola, NY, USA: Dover Publications)*
Morel, J. E., Wareing, T. A., & Smith, K. 1996, *J. Comput. Phys.*, 128, 445
Murphy, J. W., & Burrows, A. 2008, *ApJin press*, xxx
Myra, E. S., Bludman, S. A., Hoffman, Y., Lichtenstadt, I., Sack, N., & van Riper, K. A. 1987, *ApJ*, 318, 744

- Myra, E. S., & Burrows, A. 1990, *ApJ*, 364, 222
- Nomoto, K., & Hashimoto, M. 1988, *Phys. Rep.*, 163, 13
- Ott, C. D., Burrows, A., Dessart, L., & Livne, E. 2006a, *Phys. Rev. Lett.*, 96, 201102
- Ott, C. D., Burrows, A., Livne, E., & Walder, R. 2004, *ApJ*, 600, 834
- Ott, C. D., Burrows, A., Thompson, T. A., Livne, E., & Walder, R. 2006b, *ApJS*, 164, 130
- Rampp, M., & Janka, H.-T. 2000, *ApJ*, 539, L33
- . 2002, *A&A*, 396, 361
- Scheck, L., Janka, H.-T., Foglizzo, T., & Kifonidis, K. 2008, *A&A*, 477, 931
- Shen, H., Toki, H., Oyamatsu, K., & Sumiyoshi, K. 1998a, *Nucl. Phys. A*, 637, 435
- . 1998b, *Progress of Theoretical Physics*, 100, 1013
- Shlomo, S., Kolomietz, V. M., & Colò, G. 2006, *European Physical Journal A*, 30, 23
- Swesty, F. D., & Myra, E. S. 2006, submitted to the *Astrophys. J.*, astro-ph/0607281
- Thompson, T. A., Burrows, A., & Pinto, P. A. 2003, *ApJ*, 592, 434
- Thompson, T. A., Quataert, E., & Burrows, A. 2005, *ApJ*, 620, 861
- Walder, R., Burrows, A., Ott, C. D., Livne, E., Lichtenstadt, I., & Jarrah, M. 2005, *ApJ*, 626, 317
- Weinberg, N. N., & Quataert, E. 2008, *ArXiv 0802.1522 (astro-ph)*
- Wilson, J. R. 1971, *ApJ*, 163, 209
- Wilson, J. R. 1985, in *Numerical Astrophysics*, ed. J. M. Centrella, J. M. Leblanc, & R. L. Bowers, 422
- Woosley, S. E., Heger, A., & Weaver, T. A. 2002, *Rev. Mod. Phys.*, 74, 1015
- Woosley, S. E., & Weaver, T. A. 1995, *ApJS*, 101, 181
- Yamada, S., Janka, H.-T., & Suzuki, H. 1999, *A&A*, 344, 533
- Yamasaki, T., & Foglizzo, T. 2008, *ApJ*, 679, 607
- Yoshida, S., Ohnishi, N., & Yamada, S. 2007, *ApJsubmitted*
- Yueh, W. R., & Buchler, J. R. 1977, *ApJ*, 217, 565